The geometry monitoring system of the ALICE dimuon spectrometer - Overview

R. Tieulent, A. Grigoryan, J.-Y. Grossiord, H. Gulkanyan, J.-C. Ianigro, V. Kakoyan, Philippe Pillot, H. Vardanyan

EUROPEAN ORGANIZATION FOR NUCLEAR RESEARCH
European Laboratory for Particle Physics

The Geometry Monitoring System of the ALICE Dimuon Spectrometer - Overview

Authors:

R. Tieulent[1], A. Grigoryan[2], J.-Y. Grossiord[1], H. Gulkanyan[2], J.-C. Ianigro[1],
V. Kakoyan[2], P. Pillot[1], H. Vardanyan[2]

1) IPN-Lyon, IN2P3-CNRS et Université Claude Bernard, Lyon-I, France
2) Yerevan Physics Institute Br. Alikhanian st. 2, 375036 Yerevan, Armenia

Abstract:

This document was prepared for the Production Readiness Review of the Geometry Monitoring System of the ALICE dimuon spectrometer. It gives a complete description of the hardware of this system as well as its performances extracted from simulations.

Contents

Introduction

ALICE is the only experiment dedicated to the study of nucleus-nucleus collisions at the LHC. Its aim is to study the physics of strongly interacting matter at extreme energy densities, where the formation of a new phase of matter, the quark-gluon plasma (QGP), is expected. One of the most promising probes of the QGP is the production of heavy quarkonium states (J/Ψ, Ψ', Υ, Υ', Υ'') which will be detected via their leptonic decays in a forward muon spectrometer. Its tracking system consists of ten planes of cathod pad chambers. This spectrometer has to measure the invariant mass of the dimuon system with a resolution, $\Delta M_{\mu^+\mu^-}/M_{\mu^+\mu^-}$, of about 1%. In particular, in order to separate the different members of the upsilon family ($M_{\mu^+\mu^-} \sim 10$ GeV/c^2) it is necessary to have a mass resolution of about 100 MeV/c^2. In order to achieve such a resolution it is necessary to monitor the position of all tracking chambers which is the aim of the Geometry Monitoring System (GMS).

In the following, after reminding the required performances of the spectrometer, we will give a complete overview of the proposed system for the GMS.

1 Performance requirements

Mass resolution is expected to be better than 1%, corresponding to 100 MeV/c^2 around masses of the Υ family. The broadening of the mass spectrum is mainly due to the front absorber and to the tracking chambers [1]. The front absorber contribution comes from the multiple scattering with $\sigma_M \simeq 45$ MeV/c^2, the energy loss fluctuation with $\sigma_M \simeq 48$ MeV/c^2 and a mass spectrum deformation. The contribution from the tracking chambers comes from intrinsic resolutions and from multiple scattering with $\sigma_M \simeq 60$ MeV/c^2. All these quantities are given by AliRoot [2] for the Υ, and induce a total mass resolution equal to 90 MeV/c^2. As a result, in order to stay below the required 100 MeV/c^2, the contribution from the alignment of the tracking chambers to the mass resolution should not exceed 44 MeV/c^2.

In the small angle approximation, mass can be calculated using muon momenta (p) and the dimuon opening angle ($\theta_{\mu\mu}$) by:

$$M \simeq \sqrt{p_1 p_2 \theta_{\mu\mu}^2} \tag{1}$$

One can deduce the relative mass resolution as follows:

$$\frac{\sigma_M}{M} = \sqrt{\left[\frac{\sigma_{p_1}}{2p_1}\right]^2 + \left[\frac{\sigma_{p_2}}{2p_2}\right]^2 + \frac{cov(p_1, p_2)}{2p_1 p_2} + \left[\frac{\sqrt{p_1 p_2}}{M}\sigma_{\theta_{\mu\mu}}\right]^2} \tag{2}$$

In equation 2, the term $\frac{cov(p_1,p_2)}{2p_1 p_2}$ takes into account the correlation between the momenta of the two muons.

The alignment of the tracking chambers will affect the mass resolution in two different ways. First, a relative chamber mispositioning will change the bend of tracks, so the sagitta of muons, which is directly correlated to the muon momentum (using the magnetic field). The relative mispositioning will make the mass resolution worse through the term $\frac{\sigma_p}{p}$. Second, a global spectrometer mispositioning will rather change position and orientation of tracks. It will make the mass resolution worse through the term $\sigma_{\theta_{\mu\mu}}$. Nevertheless, this effect is expected to be low because the two muons will be affected in the same way (only their position relatively to the vertex will be different). As a result, the mass resolution is expected to be largely more sensitive to the chamber relative alignment efficiency, affected through the term $\frac{\sigma_p}{p}$. Therefore, equation 2 can then be rewritten as follows:

$$\frac{\sigma_M}{M} \simeq \sqrt{\left[\frac{\sigma_{s_1}}{2s_1}\right]^2 + \left[\frac{\sigma_{s_2}}{2s_2}\right]^2 + \frac{cov(s_1, s_2)}{2s_1 s_2}} \tag{3}$$

We used the fact that the sagitta of a track is inversely proportional to the muon momentum ($s \propto \frac{1}{p}$).

The two muons having opposite curvature in the magnetic field, the fake sagitta induced by chamber mispositioning will increase the momentum of one muon and decrease the momentum of the other. These two opposite effects will then lead to compensate themselves in the mass calculation. In fact, it has been shown by simulation that in cases where the errors on the momentum determination are due to alignment problem, we have:

$$\sigma_{s_1}^2 \simeq \sigma_{s_2}^2 \simeq -cov(s_1, s_2) \tag{4}$$

Therefore we can see that there are two extreme cases for the estimation of the contribution from the GMS to the mass spectrum:
- muons with momentum of the same order,
- muons with momentum largely different.
In the first case we have:

$$p_1 \simeq p_2 \Leftrightarrow s_1 \simeq s_2 \Rightarrow \frac{\sigma_M}{M} \simeq 0 \tag{5}$$

and in the case where one muon has a high momentum and the second one a small momentum:

$$p_1 \gg p_2 \Leftrightarrow s_1 \ll s_2 \Rightarrow \frac{\sigma_M}{M} \simeq \frac{\sigma_{s_1}}{2s_1} \tag{6}$$

In order to get the requirement for the alignment in terms of position (independently of the momentum of muons), we have to translate the mass resolution into sagitta resolution. We used the worst case where we have two muons with momenta largely different ($p_1 \gg p_2$). Because the mass resolution depends on the momentum of the particles, it is safe to define the requirement on the sagitta resolution using high momentum Υ, given high momentum muons. Using muons of 100 GeV/c (at the absorber end) which have a sagitta between 7 and 8 mm, we find that the contribution from the alignment to the sagitta resolution should not exceed 70 μm in order to fullfill the requirement on the

contribution to the mass resolution.

The alignment is done in two steps. First a calibration run measures the initial position of the chambers, using straight muon tracks (with the dipole magnet switched off). Then, during the physics runs, the GMS periodically measures the chamber displacements. The achieved accuracies of the calibration run were calculated by simulation [3, 4] and the following values were found: $\sigma_{\theta_{\mu\mu}} \simeq 0.1$ mrad and $\sigma_{Sagitta} \simeq 26$ μm. Taking into account these resolutions, geometrical requirement for the GMS is about 65 μm on the sagitta resolution.

2 The measurement principles

Two different types of optical alignment apparatus have been adopted for the geometry monitoring system of the dimuon spectrometer. They both derive from the RasNik system which is briefly described below. In either apparatus type the image of an object is projected on an image sensor through a lens. Then the analysis of the captured image yields a displacement measurement. In the following section we will explain the principle of these three different apparatuses.

2.1 The RasNiK's principle

The RasNiK system [5] was developed by NIKHEF for the L3 experiment. It is used by the ATLAS collaboration to monitor the position of the muon chambers in the barrel and the end-cap. Figure 1 schematizes its principle. It is a three-point imaging system where
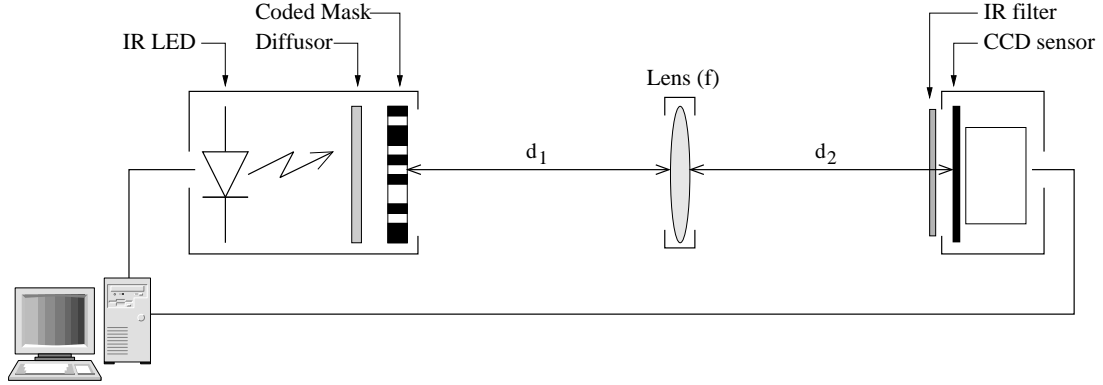
Figure 1: Basic RasNiK system.

the image of a coded mask is created on an optical sensor (CCD camera) by means of a lens, the mask being lit by an infrared LED array. Any relative displacement of one of the three elements in the X-Y plane (perpendicular to the optical axis) induces a displacement of the image seen by the CCD sensor. Relative rotation between the mask and the sensor around the optical axis can also be measured. Finally, by measuring the magnification factor (ratio between the image size and the object size), it is possible to determine the position of the lens along the optical axis.

Optimal performance requires a sharp image of the mask on the CCD. This requirement is achieved if the following relation is respected:

$$\frac{1}{f} = \frac{1}{d_1} + \frac{1}{d_2} \tag{7}$$

where f is the focal length of the lens, d_1 the distance between the mask and the lens and d_2 the distance between the lens and the CCD sensor.

The mask pattern is an alternation of black and white squares which contains encoded information every 9th row and 11th column. This information insure an unique identification of the part of the mask seen by the CCD sensor. Figure 2-left shows an example of a mask pattern. By doing a logical exclusive "or" between this mask pattern and a simple chessboard pattern, the coded information appear as shown on figure 2-right.

The best performance of this system is achieved when the magnification is close to unity (i.e. $d_1 \simeq d_2 \simeq 2f$). Given that distances between tracking stations 1, 2 and 3 on the one hand and distances between tracking stations 3, 4 and 5 on the other hand are not symmetrical, the RasNiK system is not optimal for the longitudinal monitoring of the muon spectrometer. Moreover, it has been shown that the RasNiK system alone can not provide enough constraint to monitor unambiguously five tracking chambers, whatever the number of RasNiK lines is [6], which can be extended to the entire spectrometer.
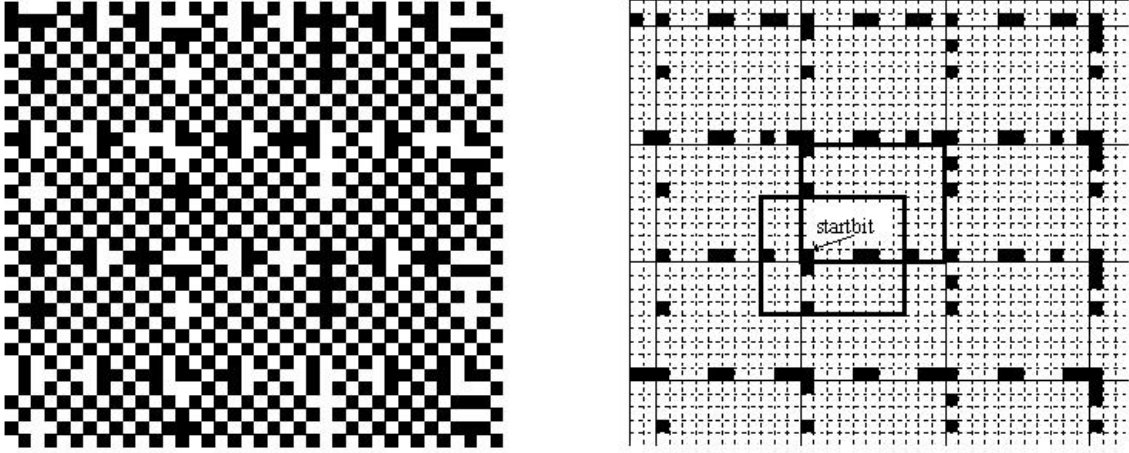
Figure 2: **Left:** Simulated coded mask, **right:** coded information extracted by logically XOR the mask pattern with a simple chessboard pattern.

The resolution of the RasNiK monitor in the transverse direction is of the order of 1 μm. The longitudinal coordinate resolution is depending on the relative distances between the CCD-lens and the lens-mask. Changes in the distances d_1 and d_2 lead to changes in the magnification of the pattern. So the resolution in the longitudinal direction is related to the resolution of the magnification measurement. Typical accuracies of a few tens of μm can be obtained.

2.2   The proximity monitor

The Proximity monitor is based on the RasNiK system. It is using the same working principle: a coded mask is seen by a CCD through a lens. The difference between the two systems lies in the fact that the CCD sensor and the lens are combined into the same enclosure (see figure 3) named the proximity telescope. The distance d_2 between the lens

Figure 3: Schematic view of a Proximity monitor.

and the CCD is of the order of 15 cm. As we said previously, the RasNiK based systems are optimal when the magnification factor is close to unity. This requirement makes the Proximity monitor suitable for short distance monitoring ($d_1 + d_2 \simeq 30$ cm). We decided to use this apparatus to monitor relative displacement of two chambers composing a tracking station.
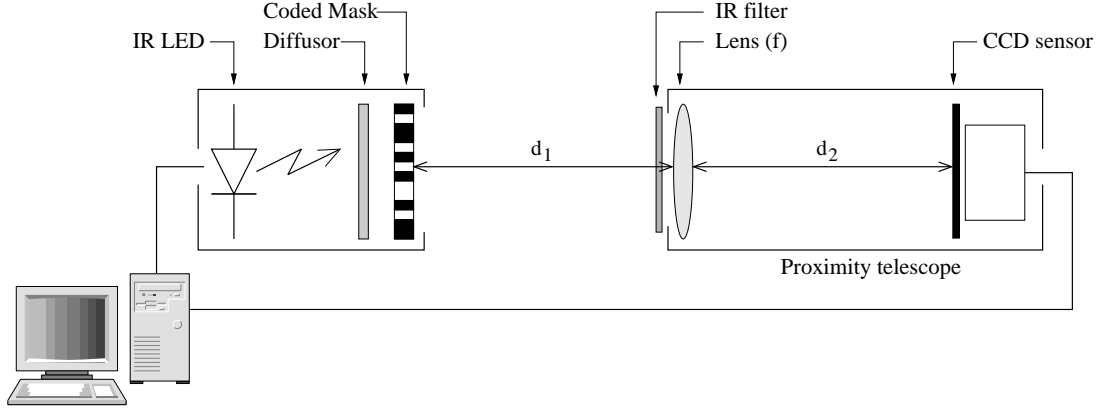
The resolution of the Proximity monitor in the transverse direction is 1 μm. The longitudinal coordinate resolution is related to the measurement of the magnification for which the resolution is of the order of 5.10^{-5}.

2.3   The BCAM monitor

The BCAM monitor [7], developed by the ATLAS collaboration, differs from the two previous devices in the object type the camera is looking at. Instead of being a coded mask, the object is a light spot. Like in the proximity case, the BCAM is a two-point imaging system since the CCD sensor and the lens are in the same box. Figure 4 gives a schematic view of the BCAM monitoring system. As it is shown in this figure, two BCAM boxes are used to form one single BCAM optical line. In fact, in addition to the CCD and the lens, a BCAM box houses two light sources (diode lasers). In that way, one BCAM box is providing two light sources for its symmetrical companion and vice versa.

As the BCAM is looking at point-like sources, the images need not to be in focus since the quantity we are interested in is the center of the intensity distribution which does not change when defocusing. Therefore, this system is very easy to implement technically as there is no need to adjust the focal length of the lens to the distance between the two BCAM boxes. Figure 5-left shows a typical image taken by a BCAM, and figure 5-right shows a zoom of the spot.
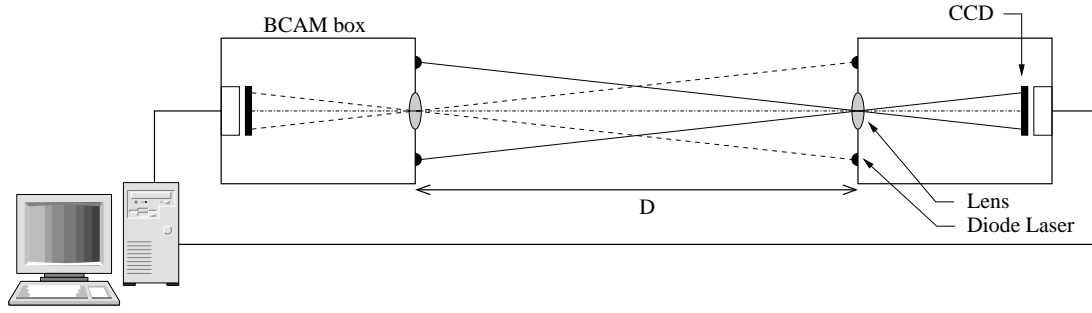
Figure 4: Schematic view of a BCAM monitor.

The center-finding precision on the CCD is about 0.5 μm. For a focal length of about 72 mm it corresponds to an angular resolution of 7 μrad over a dynamic range of 40 mrad. The distance D between the two boxes can also be extracted by a magnification measurement (using the distance between the two spots) for which the resolution is of the order of 4.10^{-4}. This device will be used in the dimuon spectrometer of ALICE to measure relative displacements of two tracking stations. It will also be used to control the movement of the platforms, supports of the optical devices, and the relative displacements of the half chamber supports of the stations 3 to 5.
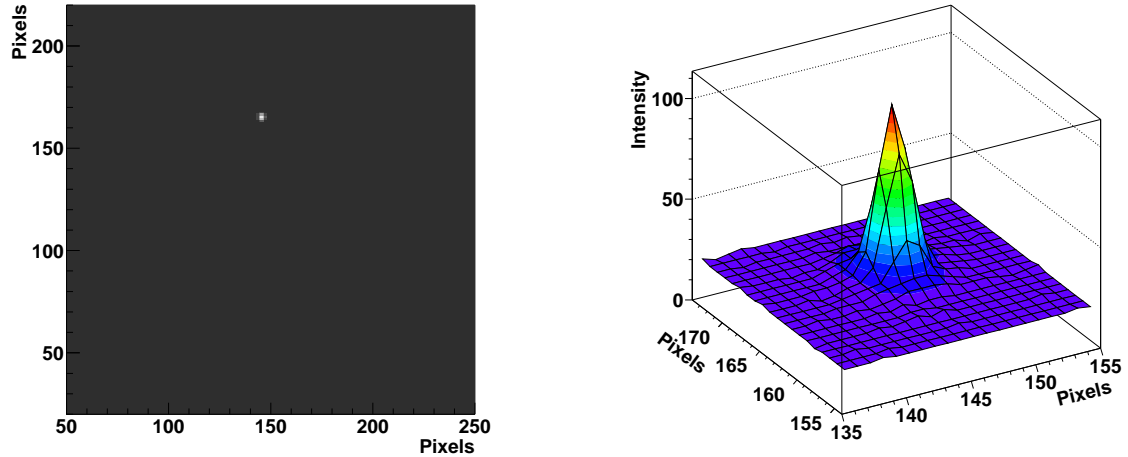
Figure 5: **Left:** Image captured by a BCAM CCD, **right:** zoom of the image spot (the z axis is the image intensity).

3 The geometry monitoring system's setup

The goal of the monitoring system is to measure the chamber displacements starting from their initial positions measured by the calibration run (with straight muon tracks). To do this, we need to install several devices (Proximity and BCAM) through the spectrometer. Their numbers and locations have been optimized by simulation in order to retreive with a good resolution the differents chamber displacement possible. Several setups were tested and only the better one is discussed in the following.
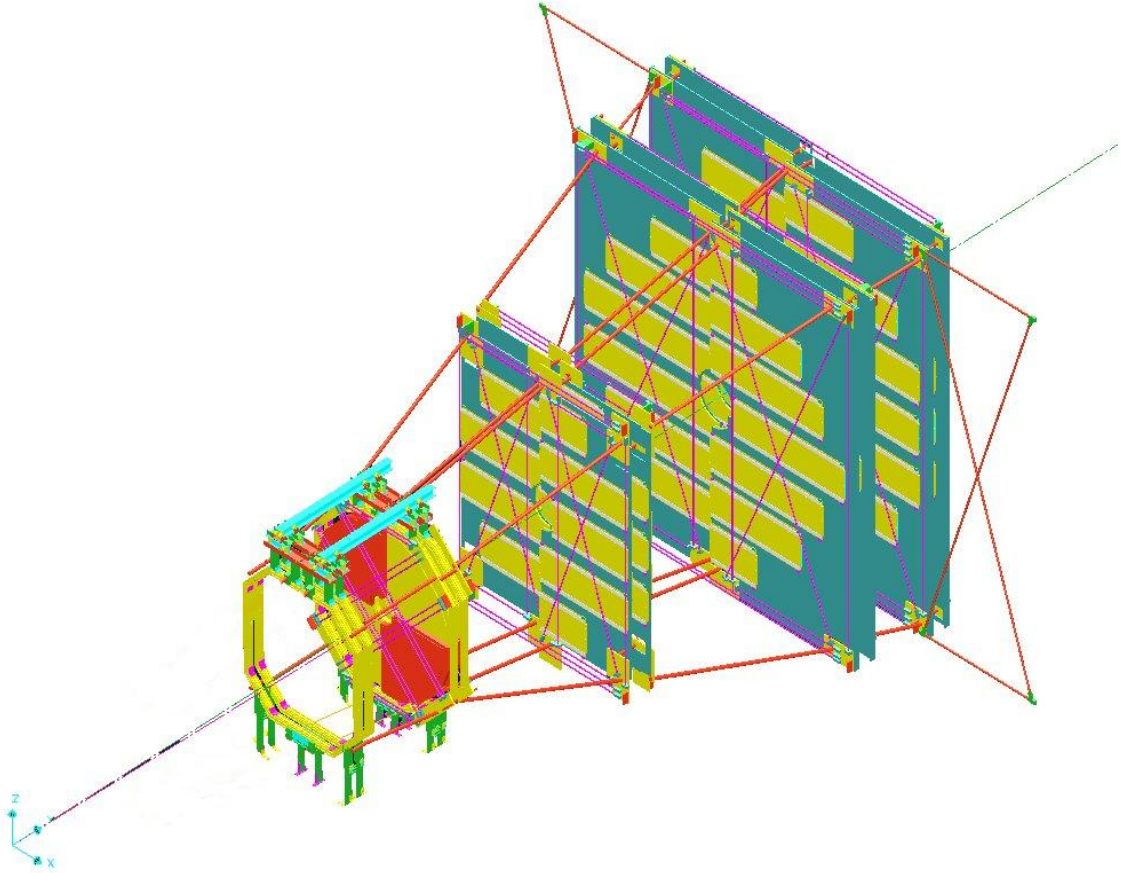
Figure 6: General view of the GMS setup. The lines on this figure materialize the optical lines but are not physical links between the tracking chambers.

In order to simplify the study, we decided to separate the project into two parts. The first one which we call the Longitudinal Monitoring System (LMS) assumes that the chambers are rigid plans. Therefore, the LMS monitors only the relative displacements of these rigid plans with respect to the others. The second part which we call the Transverse Monitoring System (TMS) has to be developed if the chambers are not rigid plans. Therefore, the TMS should give the possibility to monitor the flatness of the chambers on the chamber supports.

In this section, we first describe the LMS setup and its performance. Then we show the effect of the chamber deformation and the setup which needs to be used for the TMS.

3.1 The longitudinal monitoring system (LMS)

3.1.1 The setup

The longitudinal monitoring is composed of 8 BCAM lines between each station and 8 Proximity lines between 2 chambers of each station (see figure 7).
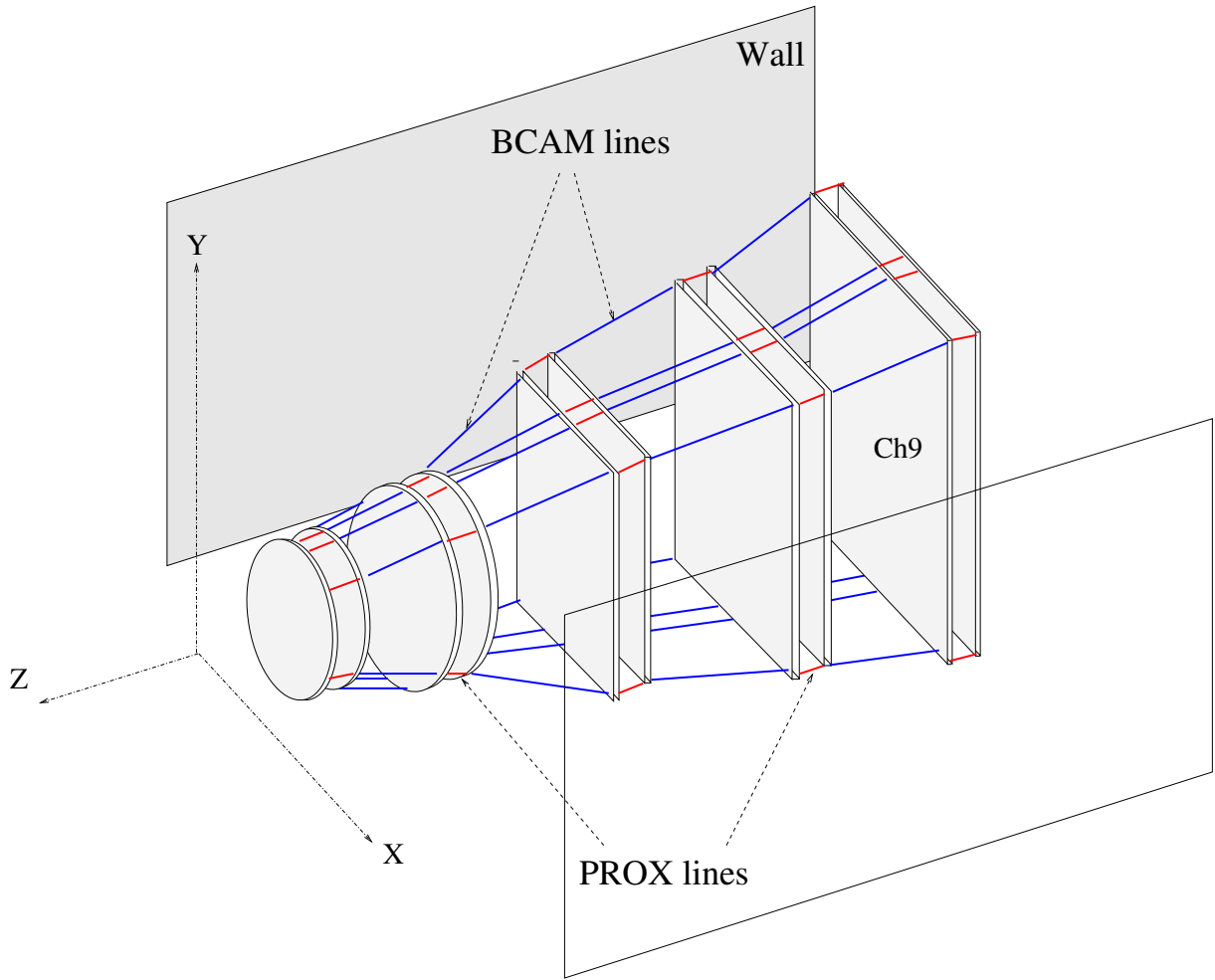
Figure 7: Schematic view of the longitudinal monitoring system setup.

This system allows to monitor all chambers relatively to the tracking chamber 9. Then we need to link this chamber to a reference (walls of the ALICE cavern) to complete the LMS. Chamber 9 has been chosen because it is the easiest one accessible from the wall of the cavern.

All optical elements are installed on platforms specially designed to orient correctly each device. A detailed description of the mechanics is given in section 7.

3.1.2   Performances of the LMS

A complete simulation of the longitudinal monitoring system was performed in order to evaluate the performances of the LMS. The detailed on that simulation can be found in a specific ALICE note [8].

The simulation procedure is as follows:

(1) Simulation of a "real" spectrometer configuration around the theoritical one using a Monte Carlo procedure,

(2) Random displacements of all chambers,

(3) Calculation of all optical line measurements (image modifications, taking into account intrinsic resolutions),

(4) Use of MINUIT (the minimization package) to extract chamber displacements. Only known quantities such as optical measurements, theoretical positions of optical lines, and chamber initial positions given by a simulation of the calibration run, are used,

(5) Comparison between induced and retrieved displacements.

Using this procedure, we were able to evaluate performances of different setups in term of position and number of optical elements. We were also able to test the best way to link the spectrometer to a reference frame, the wall of the ALICE cavern.

3.1.2.1 Internal LMS performances

The first question we tried to answer was: "What are the performances of our setup to find the relative position between two adjacent chambers?". It is what we call the "internal LMS performances". Table 1 gives the resolutions on relative position of two adjacent tracking chambers in the three directions. The internal LMS allows to measure the relative displacements of the tracking chambers

$\sigma_{i,j}$	Tracking Chamber couple : i,j = 1-10								
(μm)	1,2	2,3	3,4	4,5	5,6	6,7	7,8	8,9	9,10
σ_x	5	11	4	18	3	14	4	7	3
σ_y	6	12	4	19	4	16	4	7	4
σ_z	2	24	2	30	3	12	5	19	6

Table 1: Resolutions on relative position of two adjacent tracking chambers in the three directions (x : horizontal perpendiculary to the beam, y : vertical, and z : along the beam).

with a precision better than 20 μm in the Y direction. Using the results of table 1 we can deduce a sagitta resolution of 6.7 μm, which corresponds to a resolution σ_{M_Υ} on the invariant mass at the Υ mass of 2.7 MeV. This result is well below the requirements. We can also note from the table that Proximity sensors are more efficient than BCAMs to measure the relative displacements of chambers.

3.1.2.2 Choice of the external links

We are monitoring all chambers with respect to the vertex of the interaction. It means that any errors on the position of the first tracking chamber propagate to the last one. Therefore, an artificial global movement of the spectrometer can appear. In order to reduce this effect, we need to link the spectrometer to an outside reference at the other end. The natural reference to be used is the walls of the ALICE cavern, and the tracking chamber 9 is the easiest chamber to link to the walls.

It is possible to control the vertical displacement (in the bending direction of tracks) of the chamber 9 relative to the walls using the setup shown by figure 8[a]. We simulated this setup using RMS values of 1 mm and 1 mrad for the long term wall deformations [9] (physical runs will go on during several months without any calibration).

---

[a] A detailed discussion on the choice of this setup can be found in reference [8].
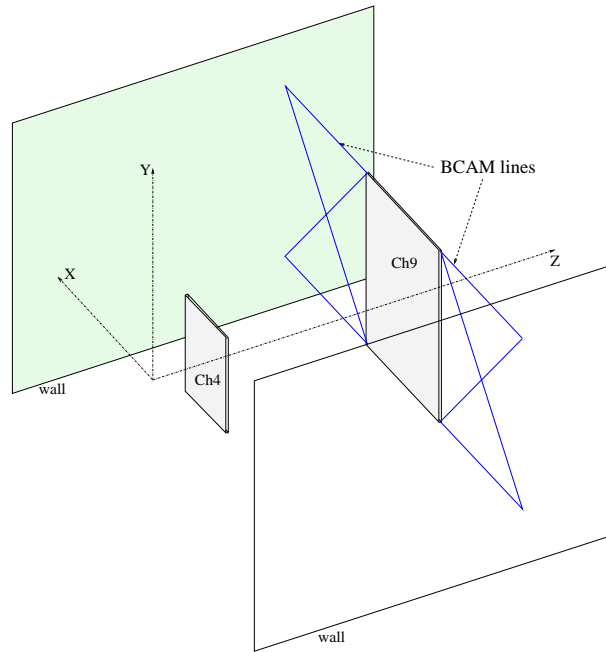
Figure 8: Schematic view of the setup of the external links.

In order to evaluate the performances of the external monitoring, several quantities can be evaluated:

- reconstruction accuracies of tracking chamber 9 displacements (3 translation and 3 rotation parameters),
- effect on the Υ mass resolution which can happen through momentum and opening angle resolutions of the two muons,
- effect on the Υ transverse momentum and rapidity resolutions.

Table 2 gives the results of this simulation. The first line in Table 2 is the reference: external monitoring is perfect so results come only from internal monitoring and are the same as in the previous section. The second line of this table gives the resolutions achieved when the external monitoring is done using the setup described in figure 8. The first two columns give the resolution of the position Y and angle θ_z (rotation around the Z axis) of the tracking chamber 9 relative to the walls.

Displacements of all chambers can be found relative to the tracking chamber 9, so a bad displacement measurement of this one can affect all tracking chambers in the same way. It means that the position of the entire spectrometer can be badly determined, but the relative position accuracies of chambers can not be affected. This is what we can see in Table 2. Only variables depending on the global position of the spectrometer (Pt_Υ and Y_Υ) are really affected whereas the resolution in σ_p (depending mostly on chamber relative position) is almost not. The opening angle between the two muons at the absorber end is not affected a lot by the global displacement of the spectrometer, because it only depends on the relative position of the reconstructed tracks. Nevertheless, the opening angle reconstructed at the vertex ($\alpha_{\mu\mu}$) is calculated using the Badier-Brandson method [1] which uses both the angle and the position of the muons at the absorber end. Because the relative position of the two muons at the absorber end is affected by a global displacement of

the spectrometer (particulary in the beam axis direction), the opening angle at the vertex is affected too (column 4 in Table 2).

setup	σ_y	σ_{θ_z}	$\frac{\sigma_p}{2 \cdot p}$	$f \cdot \sigma_{\alpha_{\mu\mu}}$	σ_{M_Υ}	σ_{Pt_Υ}	σ_{Y_Υ}
	(μm)	(μrad)	$(\times 10^{-4})$	$(\times 10^{-4})$	(MeV/c^2)	(MeV/c)	$(\times 10^{-4})$
Int. only	0	0	3.2	0.1	2.6	6.4	1.6
Int. + Ext.	545	47	3.6	1.6	3.2	47	20

Table 2: Effects of external links on several quantities : reconstruction accuracies of tracking chamber 9 displacements (position y and angle θ_z), relative momentum, opening angle, Υ mass, transverse momentum and rapidity, using AliRoot ($f = \frac{\sqrt{p_1 \cdot p_2}}{M_\Upsilon}$).

In order to give a definitive result of the monitoring system, it is important to compare the contributions to the resolution given in Table 2 to the contribution to the resolutions due to the front absorber and the tracking chambers themselves which are for Pt_Υ and Y_Υ 60 MeV/c and 77.10^{-4}, respectively. We can see that the monitoring system is able to achieve a resolution which does not change the intrinsic resolution of the dimuon spectrometer very much.

3.2 The transverse monitoring system (TMS)

All the simulations which were performed for the study of the LMS assumed that the tracking chamber supports were rigid plans. We first study the effect of plan deformations on the LMS resolution. As the elements which compose the LMS are fixed to platforms at the corners of the chamber supports, only the deformations which rotate or displace a corner relative to the others have an effect on the LMS.

Therefore, we simulated deformation of the chambers by allowing displacements and rotations of the platforms. The displacements and rotations were at the 1 mm and 1 mrad levels. In order to give an order of magnitude, these numbers correspond for a chamber support of station 5 to a sagitta of 3 mm over the 6 m of its length.

Figure 9 shows a schematic of the two easiest deformations a support plan can experience. We simulated the LMS using these parameters and extracted the resolution on the sagitta determination of muon tracks. We found $\sigma_{sagitta} \simeq 700$ μm which corresponds to about 250 MeV/c^2 on the mass resolution at the upsilon mass (see figure 10). This resolution is by far bigger than the requirement which is about 67 μm (see section 1). It is clear from this study that a system which monitors the planearity of the chamber's support is needed. In the fol-
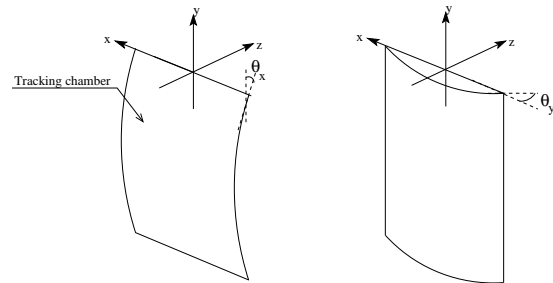

Figure 9: Schematic view of the two easiest deformations that a support plan can experience.

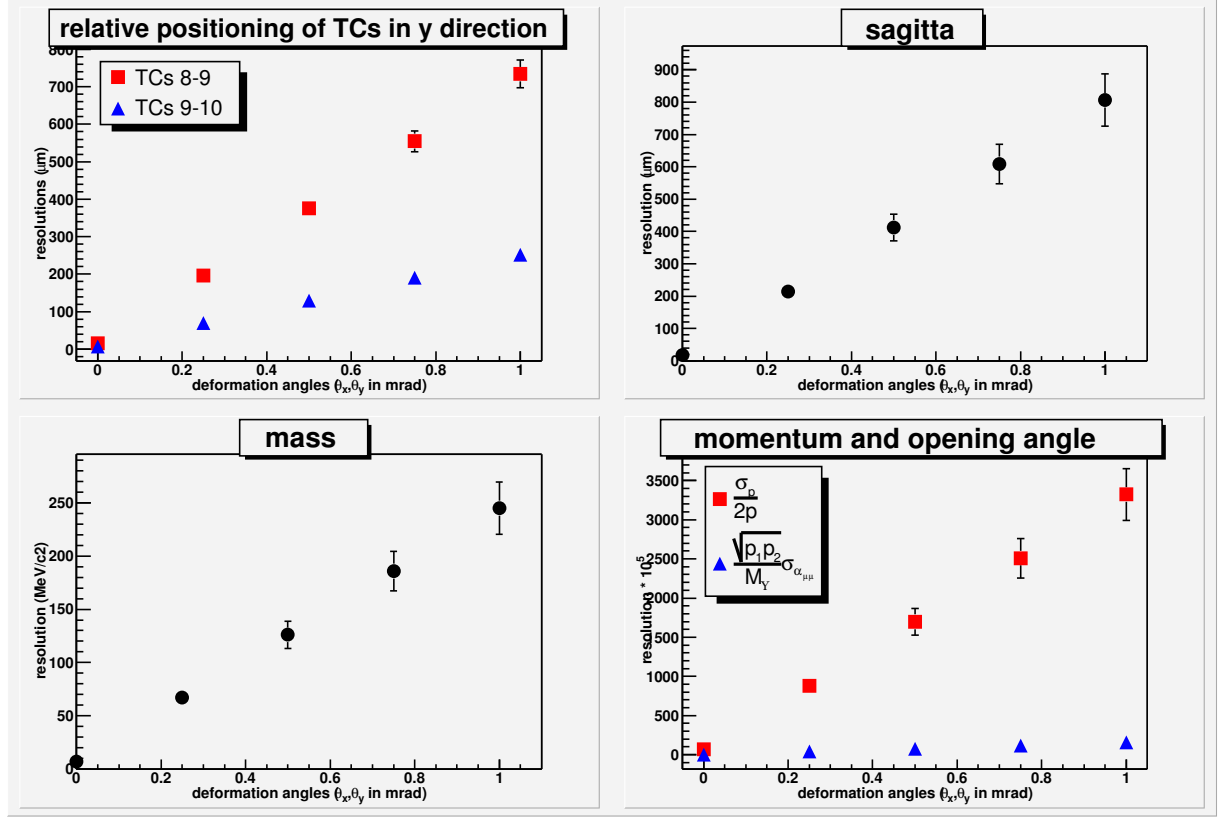lowing we present the proposed setup and its performances.

Figure 10: Effects of plane deformation on several quantities: **top left:** relative positioning accuracies between tracking chambers 8-9 (monitored by BCAMs) and 9-10 (monitored by PROXs) in the bending direction, using straight lines uniformly distributed in the spectrometer acceptance; **top right:** false sagitta induced on these straight lines; **bottom left:** Υ mass resolution; **bottom right:** relative momentum ($\frac{\sigma_p}{2 \cdot p}$) and opening angle ($\frac{\sqrt{p_1 \cdot p_2}}{M_\Upsilon} \cdot \sigma_{\alpha_{\mu\mu}}$), using AliRoot.

3.2.1   Setups of the transverse monitoring system
Due to the two different configurations used for the tracking stations, we developed two different setups for the transverse monitoring system.

3.2.1.1   Setup for chambers of stations 1 and 2   Figure 11 shows a schematic view of the setup used to monitor the planearity of the chamber supports of stations 1 and 2. An array of BCAMs (black rectangles) gives the possibility to determine the relative orientation and position of the four platforms which support the optical elements. These relative orientation controls are needed to achieve a good resolution for the longitudinal monitoring.

The chambers have the shape of one quarter of a disk (see figure 11). They are fixed to the support only at their outer radius. On the inner radius side (close to the beam pipe) they are free to move. Bi-directional diode laser sources (grey points in Fig. 11) placed on the chambers in the field of view of the BCAM which are on the platforms will give
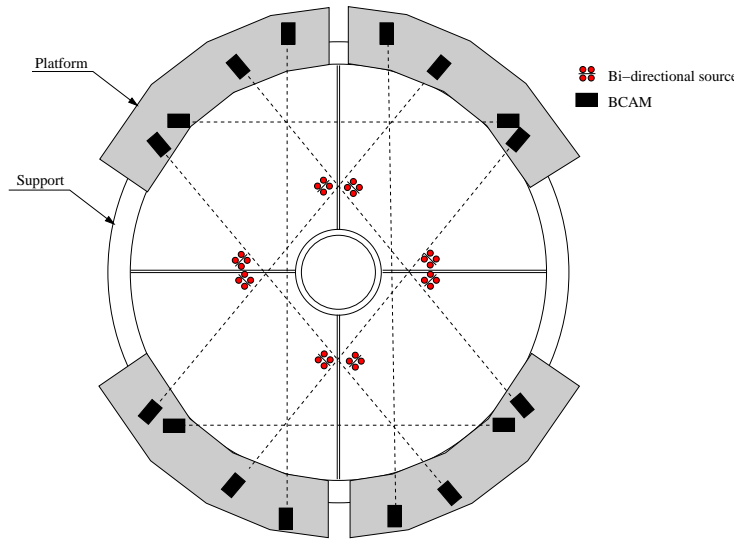
Figure 11: Schematic view of the transverse monitoring for chambers of stations 1 and 2.

us the possibility to determine the movement of the quadrants along the beam axis. The bi-directional sources are installed on the radial dead zone of each quarter as indicated in Fig. 11.

3.2.1.2   Setup of stations 3, 4 and 5   Figure 12 shows a schematic view of the setup used to monitor the planearity of the chamber supports of stations 3, 4 and 5. The array of BCAMs controls the relative orientation and displacement of the eight platforms with respect to the chamber theoretical plan. Therefore, it gives the information about the position of the four corners of each chamber support. The BCAM boxes which are on the center platforms are named "double" BCAM. On both faces, they have 2 laser diodes and one CCD which allow them to "look" and "shine" in both directions.

In order to find a basic shape of the chamber support one needs more points on the surface of the support. As for stations 1 and 2, we are using bi-directional diode laser sources glued on the chambers support. The bi-directional sources are in the field view of the BCAM which are on the platforms. Thus using this setup, we know the position of nine points of each chamber support.

3.2.2   Performances of the transverse monitoring system

We evaluated the performances of the transverse monitoring system by simulation. We used the same strategy that was used for the longitudinal monitoring system: induce plan deformation (i.e. rotation and displacement of the platforms) and recalculate those deformations from the image of each sensor.

A support plan can experience very complicated deformations which change the orientation and the position of the platform set at each corner of the supports. As it is depicted in Fig. 9 the most significant deformations that a plan can experience are torsion around the X axis (horizontal transverse to the beam axis) and the Y axis (vertical). The two different torsions induce change in the rotation angles θ_x and θ_y of the platform and also in their Z positions along the beam axis.
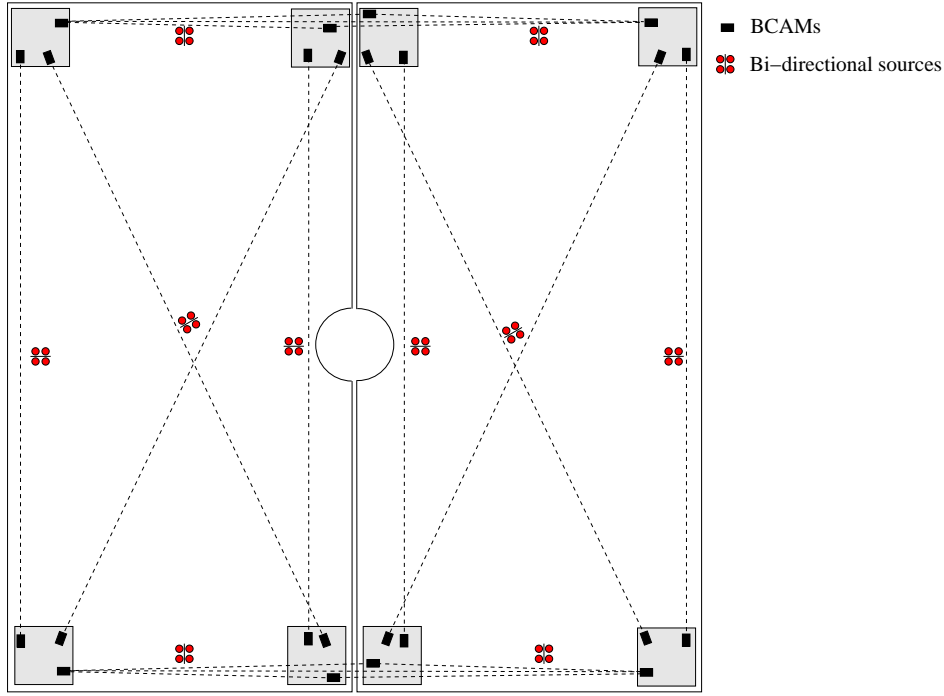
Figure 12: Schematic view of the transverse monitoring for stations 3, 4 and 5.

In order to simulate any plan torsions, we randomly chose rotation angles θ_x and θ_y and position Z of each platform and tried to extract back them using the image given by each sensor. Table 3 gives the sigma of the residuals between the induced and the retrieved movements of the platforms. We can see that the TMS is able to monitor the rotation angles of the platform at the level of 8 μrad. One can notice that the resolution achieved on the rotation angles is constant as a function of the station number. At the opposite, it is not the case for the resolution on the displacement along the Z axis. We can explain easily that σ_z grows with the station number due to the fact that the distance between the platform get bigger as we go from station 1 to station 5. The angular resolution of the BCAM being constant, makes the position resolution bigger when the size of the system increases.

Station	σ_{θ_x} (μrad)	σ_{θ_y} (μrad)	σ_z (μm)
1	8.4	8.3	8.5
2	8.0	8.1	10.2
3	7.9	8.3	17.3
4	8.4	8.0	28.1
5	8.2	8.6	31.2

Table 3: Performances of the transverse monitoring system using the intrinsic resolutions of the optical devices.

Using this setup for the TMS and the intrinsic resolution of the optical devices, we extracted the resolution on the sagitta determination for muon tracks. We found a resolution $\sigma_{sagitta}$ of 16 μm which is below the requirements given in section 1.

4 Simulations of effects of external parameters on the GMS efficiency

4.1 Effects of the optical element installation accuracies

A very important point of our procedure is that we measure chamber displacements and not directly chamber positions. As a result, optical elements have not to be placed with a very high accuracy because we are not interesting in the absolute position of images on CCDs but only in the image displacements relative to the reference images. Effectively, because of these references are also affected by the optical element mispositioning, image displacements are almost not. For example, any BCAM's LED translation parallel to the CCD plan induces the same measurement whatever the initial position of the LED is in this plan. However, a bad knowledge of the relative orientation or position of the two boxes along the axis perpendicular to the CCD plan may induce a wrong interpretation of any displacements. As a result, even if the image displacements are less affected than their
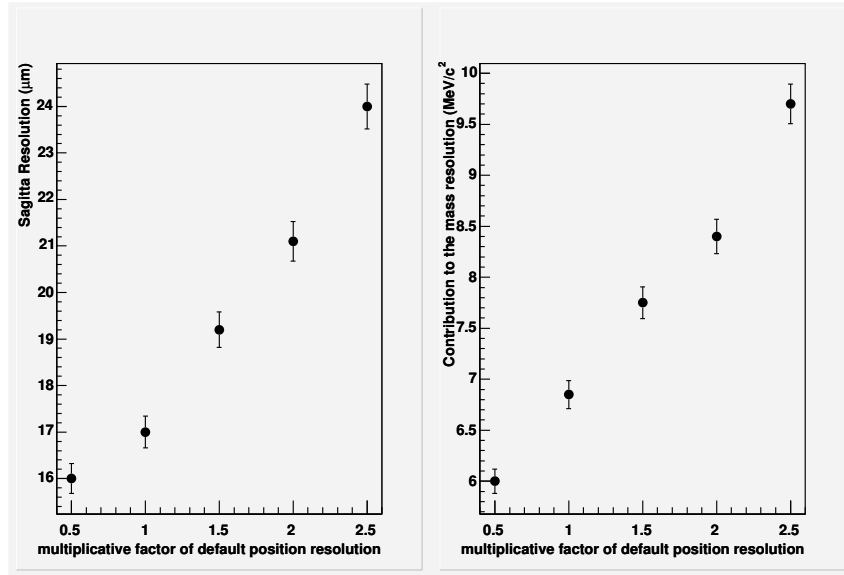
Figure 13: Effects of optical element mispositioning **left:** on false sagitta induced on straight tracks ; **right:** on Υ mass resolution.

absolute positions, real effects and requirements on optical element positioning accuracy must be evaluated by simulation. Intrinsic resolutions of the optical systems are fixed to their nominal values (given in section 2), and only the internal monitoring, which is the most sensitive one, is simulated (the 6 displacement parameters of tracking chamber 9 are fixed to their "real" values).

We can see on plots shown in Fig. 13 that resolutions on sagitta and mass are not affected much by the optical element mispositioning. With 0.5 mm and 0.5 mrad inaccuracy in all directions, fake sagitta is only around 16 μm and the contribution of the GMS to the mass resolution is about 6 MeV/c^2.

In situ, the installation of the elements will be done in two steps. First, they will be mounted as well as possible in order to respect the optical acceptances of systems (each CCD must look at its mask or its LEDs). Second, their exact position relatively to their chamber plan will be measured. It has been shown in this section that no specific requirement for measuring accuracies has to be done. Position and orientation of all optical elements can easily be measured with a precision better than 1 mm and 1 mrad respectively using the photogrammetry.

4.2 Effects of the optical system intrinsic resolution

Figure 14: Effects of intrinsic resolution on several quantities: **top left:** relative positioning accuracies between tracking chambers 8-9 (monitored by BCAMs) and 9-10 (monitored by Proximities) in the bending direction, using straight lines uniformly distributed in the spectrometer acceptance; **top right:** false sagitta induced on these straight lines; **bottom left:** Υ mass resolution; **bottom right:** relative momentum ($\frac{\sigma_p}{2 \cdot p}$) and opening angle ($\frac{\sqrt{p_1 \cdot p_2}}{M_\Upsilon} \cdot \sigma_{\alpha_{\mu\mu}}$), using AliRoot. Default resolutions are the values presented in section 2 (description of optical elements).

The GMS efficiency of course depends on the intrinsic resolutions of the optical devices.

These ones are affected by thermal gradients and fluctuations [7, 10, 11] which append close to the electronics of the chambers.

We evaluated by simulation the tolerance of the monitoring system toward the decreasing of optical system resolution in order to know if something has to be done according to the results of the test described in section 9.1. In this simulation, only the monitoring of the relative position of the chambers, which is the most sensitive one, is simulated (the 6 displacement parameters of tracking chamber 9 are fixed to their "real" values).

Results of the simulation are shown in Fig. 14 where resolutions on various geometrical and physical quantities are plotted versus the resolution of the optical elements which is expressed as a factor of the intrinsic resolutions.

The resolution on sagitta determination (see Fig. 14-top-right) becomes higher than requirements if the resolution of the optical elements is about four times the intrinsic one. It implies that some remedy is needed if effects of thermal gradients and thermal fluctuations go beyond this limit. Tests were conducted in the laboratory to determine the comportment of the BCAM resolution in presence of the thermal fluctuations. These tests are presented in section 9.1.

4.3 Effects of device's breakdowns

We tested by simulation the robustness of the system against breakdowns of optical devices. In order to do so, we artificially shutdown one or more optical lines inside the system and tried to extract induced displacements and deformations using this uncomplete system.

4.3.1 Effect on the longitudinal monitoring system

The effects of devices's breakdowns on the performances of the LMS were simulated by removing randomly a given number of optical lines between two adjacent tracking chambers. When these lines are BCAM, removing one line means removing the four images given by the four laser diodes. Figure 15 shows the results of this simulation. Several geometrical and physical quantities are plotted versus the number of breakdowns between two adjacent chambers. As expected, the resolution on the mass and the sagitta deteriorates as the number of breakdowns between two adjacent chambers increases. This simulation was conducted with three times the intrinsic resolution of the optical devices in order to take into account the effects of thermal fluctuations.

As we mentionned in section 3.1.1, two adjacent chambers are linked together by 8 optical lines (either 8 BCAM or 8 Proximity). Therefore, one can see that when only one out of eight lines (BCAM or Proximity) breaks the loss in resolution is relatively small (see Fig. 15-top-right). With four breakdowns out of eight lines, the loss in resolution is fairly big with in addition a loss in efficiency of 11% due to errors in the minimization procedure. We can conclude that the system is robust to breakdowns as even with three breakdowns out of eight lines the resolution on the sagitta is still below the requirements.
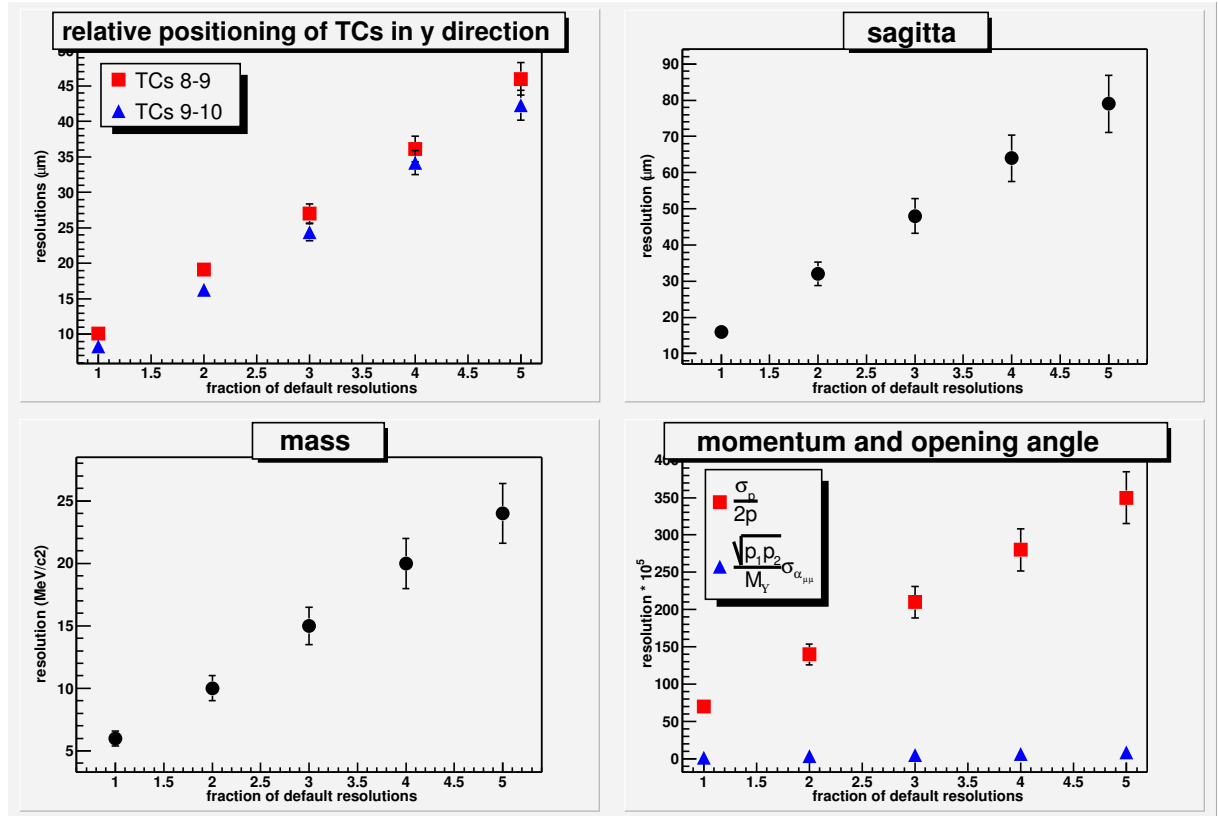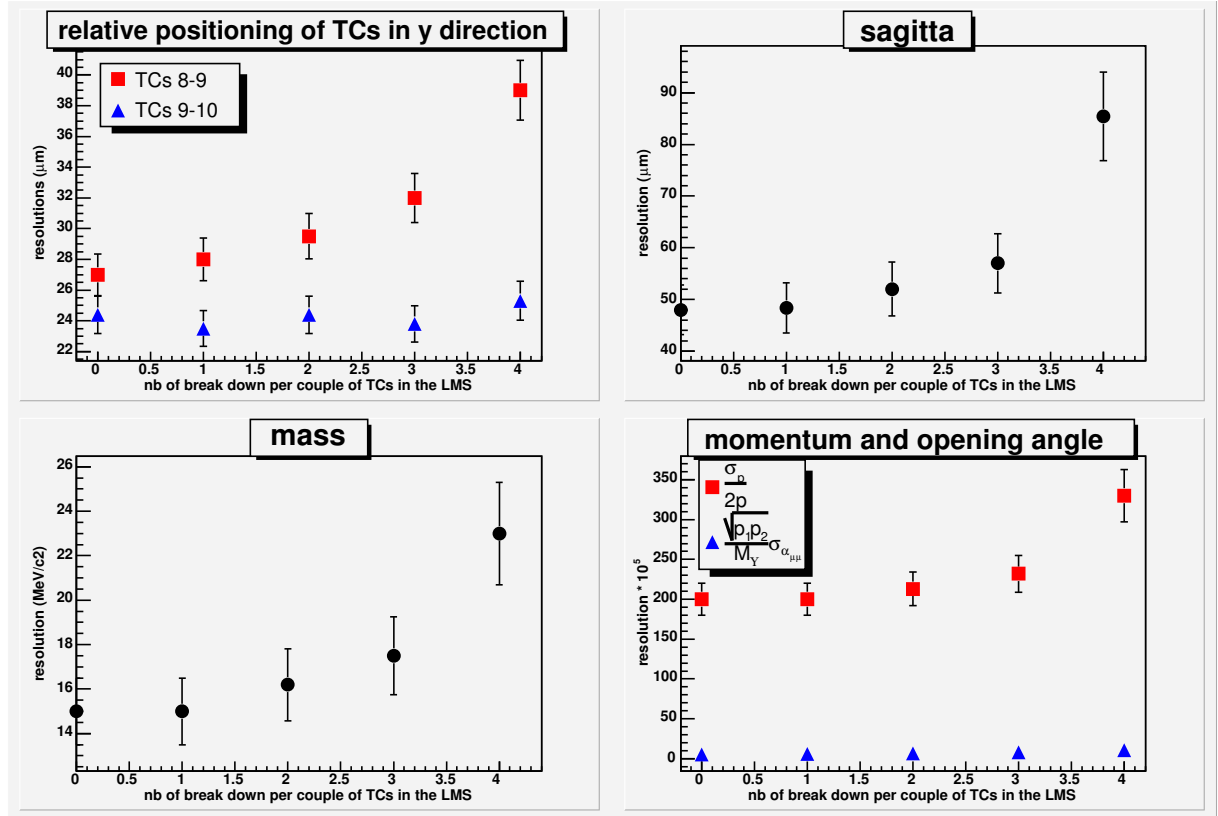
Figure 15: Effects of breakdowns on several quantities: **top left:** relative positioning accuracies between tracking chambers 8-9 (monitored by BCAMs) and 9-10 (monitored by Proximities) in the bending direction, using straight lines uniformly distributed in the spectrometer acceptance; **top right:** false sagitta induced on these straight lines; **bottom left:** Υ mass resolution; **bottom right:** relative momentum ($\frac{\sigma_p}{2 \cdot p}$) and opening angle ($\frac{\sqrt{p_1 \cdot p_2}}{M_\Upsilon} \cdot \sigma_{\alpha_{\mu\mu}}$), using AliRoot.

4.3.2   Effect on the transverse monitoring system

We looked at the effect of device's breakdowns on the performances of the TMS. We redid the simulation we made in section 3.2.2 to determine the performance of the TMS described. This time, we artificially removed some optical lines in order to mimic breakdowns. The lines we removed were chosen randomly.

Figure 16 gives the results of this simulation. It shows the resolutions obtained by the TMS on the platform angles θ_x and θ_y and position Z as a function of the tracking station tested and the number of device's breakdowns per chamber. The simulation was conducted with three times the intrinsic resolution of the optical devices in order to take into account the effects of thermal fluctuations. Therefore, the results without breakdown are compatible with the results given in table 3 multiplied by a factor 3.

From the results shown in Fig. 16, we can see that the system is fully working (no loss due to minimization errors) if only one breakdown occurs in a given chamber (or half chamber for stations 3 to 5). The detoriation of the resolution is bigger for stations 3 to 5 than for stations 1 and 2. This is due to the fact that 8 BCAM lines are used in the setup for station 1 and 2 (see Fig. 11) rather than 6 in the setup for stations 3 to 5 (see
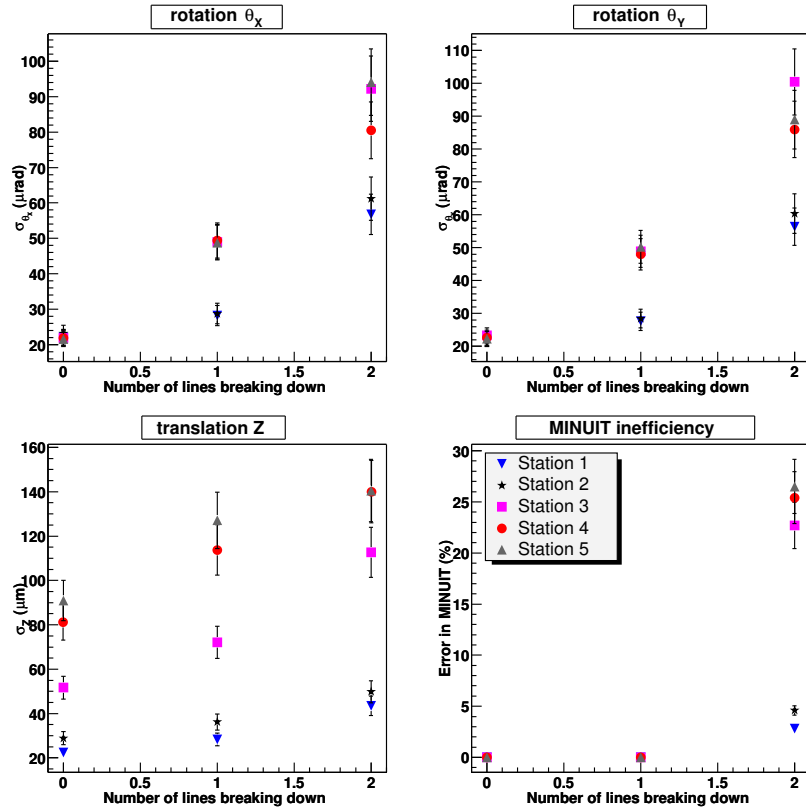
Figure 16: Resolution obtained by the TMS on the platform angles θ_x and θ_y and position Z as a function of the tracking station tested and the number of device's breakdowns per chamber (or half chamber for stations 3 to 5). The simulation has been conducted with three times the intrinsic resolution of the optical devices in order to take into account the thermal effect.

Fig. 12) to monitor the same number of platforms.

When we go to two breakdowns per chamber, errors during the minimization procedure occur and the resolutions deteriorate a lot for all stations.

Table 4 shows the degradation of sagitta and mass resolution as a function of the number of breakdowns per chamber in the TMS setup.

# device's breakdowns per chamber	$\sigma_{sagitta}$ (μm)	σ_M (MeV)
0	48	15
1	68	21
2	112	35

Table 4: Resolution on the sagitta and the Υ mass as a function of the number of device's breakdowns per chamber in the TMS setup (or half chamber for stations 3 to 5).

5 Electronics

In this section we detail the front-end electronics of the GMS. It was developed by the Brandeis University for the ATLAS Muon end-cap alignment [b].
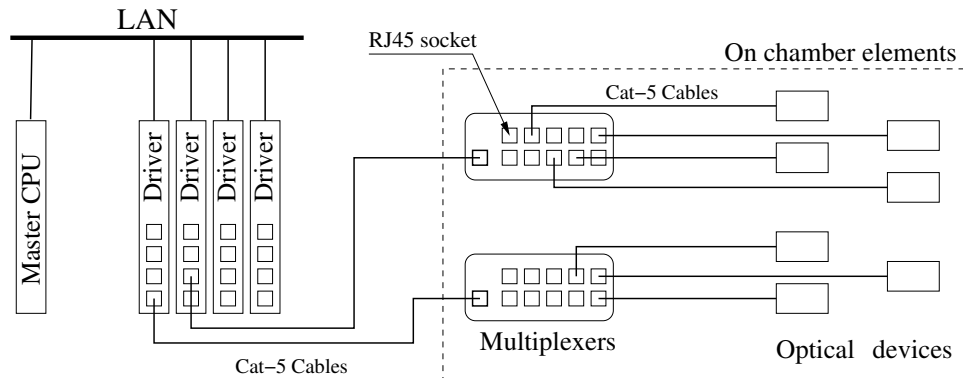

Figure 17: Schematic of the data acquisition system. The optical device can be one of the devices we describe further in this section.

5.1 The driver board and the multiplexer
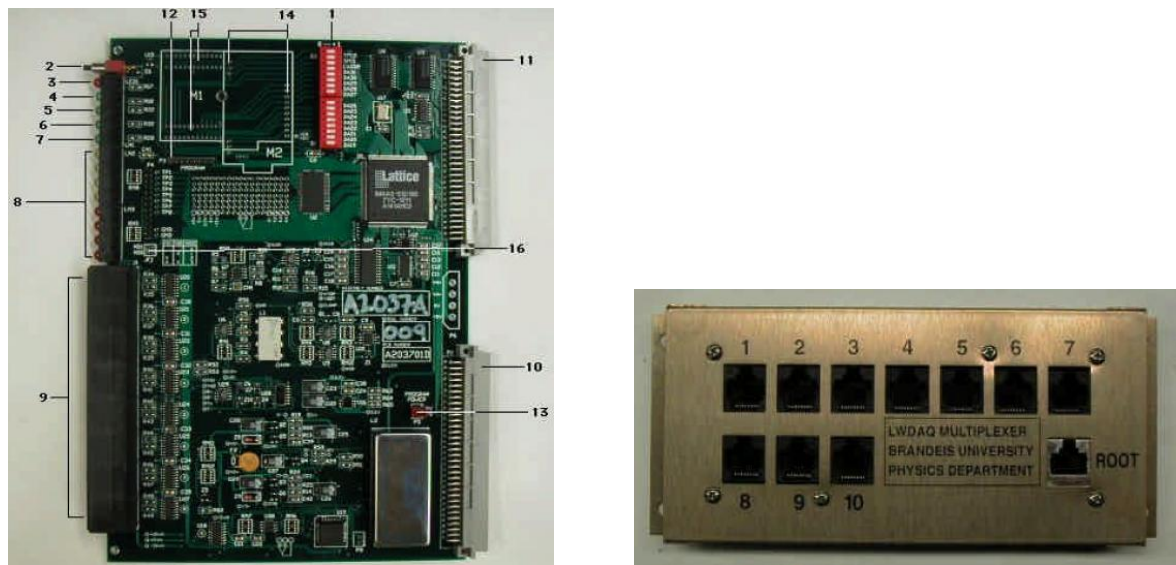
Figure 18: **Left:** the driver board, **right:** the multiplexer.

Figure 17 schematizes the layout of the front-end electronics. All optical devices (CCD sensors, Diode Lasers, LED arrays) are connected to a driver board through a multiplexer. Each driver board (see figure 18-left) provides 8 input-output sockets through which it transmits commands to the devices, provides low voltages and receives data. The driver boards provide timing for CCD readout, and times source flashes. It stores digitized images

---

[b] The manual of each electronics device we describe in this section can be found on the following web site : http://alignment.hep.brandeis.edu/ATLAS/Electronics/

in a 512 kbytes RAM. The Master CPU coordinates the data acquisition, gets the images from the RAM of the drivers, analyzes them and sends the result to the minimization procedure.
In order to save space and cables, ATLAS collaborators developed a multiplexer (see Fig. 18-right) which provides ten branch sockets per root socket. The multiplexers will be mounted on the chamber support frames.

5.2   The CCD sensor

The image sensor used is the CCD sensor TC255P manufactured by Texas Instruments [12]. The image-sensing area of the TC255P is made of 243 lines with 324 pixels in each line. Each pixel is $10 \times 10~\mu m^2$. The CCD sensor is connected to its driving electronics board by a eight-way flex cable which can be up to 300 mm long (see Fig. 19). The electronics board receives a 16-bit command from the driver board. This command can be of different type: turn on/off the CCD, move the image to the storage area of the CCD, transfer the image to the driver, etc. The driving board returns the data to the driver for later analysis. This device can be in two modes, asleep or awake, for which the power consumption is respectively 13 mW and 1.2 W.
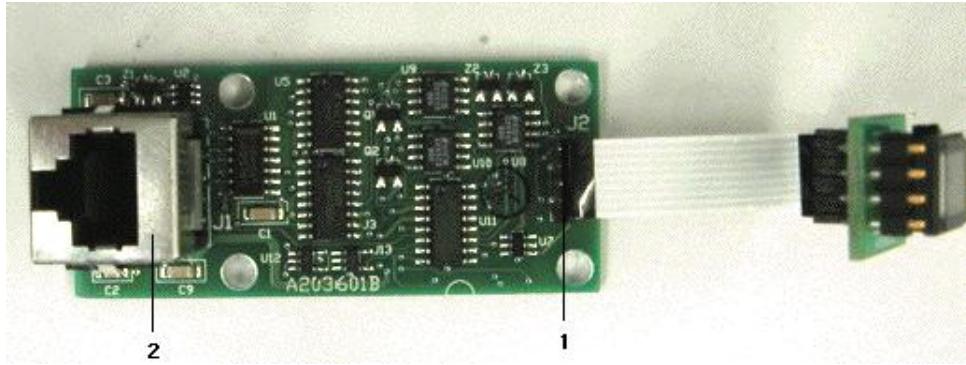

Figure 19: The CCD sensor connected to its readout electronics by a eight-way flex cable (1). A RJ45 socket for connection to a driver board or to a multiplexer (2). Dimensions of the readout board: 63×28 mm.

The TC255P was tested for radiation hardness [13]. The effect of fast neutron irradiation is an increase of the CCD dark current. The dark current for a given CCD is really stable from one image to the next. So as long as the pixels do not fill up to saturation with dark current, it is possible to remove it by subtracting an image taken with the dark current only (this is done taking an image without turning on the light source). ATLAS collaborators showed that the TC255P can endure a dose up to 3.7×10^{13} (1 MeV equiv. neutron/cm^2) which is about a factor 300 bigger that the maximum expected cumulative dose in the ALICE dimuon spectrometer for ten years of operation [14].

5.3 The coded mask

The coded mask provided by the ATLAS collaboration (see Fig. 20) is illuminated by an array of light-emitting diodes (LED). It has nine infra-red LEDs (part number HSDL-4400 from HP). The power consumption of this device is 17 mW in the asleep mode (LEDs off) and 2.4 W in the awake mode (LEDs on).
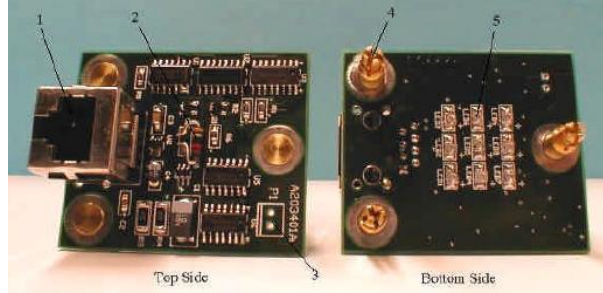

Figure 20: The LED array which lits the coded mask. The RJ45 socket for connection to a multiplexer (1). Three snap-in standoff to fix the coded mask (4). Infra-red LEDs (5).

The LED array was tested for radiation hardness [15] by irradiation with γ-ray, fast neutrons and energetic protons. The effect of radiation is a reduction in the light output. No significant loss in the light output was noticed for irradiation by γ-ray with a dose of 377 Gy. The LEDs are more sensible to the damage caused by fast neutrons. A loss of 80% in output power was observed after a dose of 10^{13} (1 MeV equiv. neutron/cm ^{2}) which is about 100 times the maximum expected cumulative dose in the ALICE dimuon spectrometer for ten years of operation [14].

5.4 The BCAM

The BCAM box provided by the ATLAS collaboration (see Fig. 21) includes one CCD sensor (of the same type that the one used for the Proximity device), one lens of focal length 72 mm and two laser diodes as light sources. As it was explained in section 2.3, two BCAM boxes are used to form a single BCAM line. The lasers of one box are seen by the CCD of the other box. The laser diodes used are are from Sanyo with the part number DL3147 which emit visible light at a wave length of 645 nm. The output power of each laser diode is 7 mW with a beam divergence of 30°. The laser pulses have a typical time length of 10 μs in order to be detected by the CCD. The power consumption of the BCAM is 14 mW when the device is not active, and 1.2 W when the CCD or one of the lasers is turned on.

The lasers were exposed to 10^{13} (1 MeV equiv. neutron/cm ^{2}) to test their radiation tolerance. A 10% reduction in the output power was measured [16]. These lasers were also exposed to ionizing radiation dose of 1000 Gy and no change was measured in the output power. Therefore we can conclude that lasers are resistant to radiation.
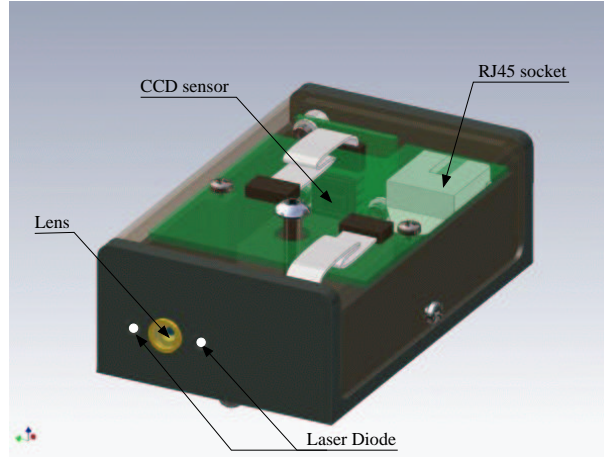
Figure 21: View of the BCAM box.

6 Data acquisition

Figure 22 shows a schematic view of the DAQ architecture. As it was described in the section 5, all optical elements (BCAM, Proximity) are connected to multiplexers which are connected to Driver boards (see Fig. 17).

A program running on the Master CPU will continuously acquire images from the optical elements. In order to acquire images in the proper order and to switch on the laser or mask in front of the corresponding CCD, we should have a database which gives a complete description of the cabling to the acquisition program. This database is named "input database" in the schematic of figure 22. This database is loaded once for all when the system starts. It contains information related to the cabling, the position of each element and also the exposition time needed by each optical line to acquire an analyzable image. The "image acquisition" program continuously acquires images in a predefined order and analyse them. A background subtraction is possible by subtracting from the image acquired with the laser (or mask) switched ON an image acquired with the same exposure time but with the laser (or mask) turned OFF. This subtraction is done by the "image analysis" software. When the "image analysis" software is done with the analysis of all the images of a complete cycle, it makes a new entry in the "output Database". It also sends the results of the image analysis to another CPU which handles the minimization procedure. This procedure retrieves the chamber displacements and deformations from the image displacements. We named this program the "minimization" software. We also record into the output database the image when the "image analysis" failed in order to be able to diagnose later on the cause of the image analysis failure. When the "minimization" is done, one entry is made in the "output database" which contains the displacement and deformation of the chamber supports. We decided to do at each cycle one entry with the results of the image analysis in order to be able to do an offline re-analysis of the data if needed. The online version of the "minimization" is just for diagnostics.

In the control room, a program running under PVSS gives the possibility to the user to control the entire system. It will be possible to turn on or off the entire system, display

Figure 22: Schematic view of the data acquisition chain.

the images, check the results of the analysis of a given image. We should also be able to change the exposure time in order to have brighter or darker images, as well as check the result of the minimization.

A total of 1128 images will be acquired for each cycle (half of them are for background subtraction). It takes about 5 minutes to acquire and analyse all the images of a complete cycle which is long enough for the "minimization" software to retrieve the positions and deformations of the chambers and to enter the result in the output database.

7 Mechanics and integration

This section presents mechanical drawings of different elements of the system and several solutions adopted for the integration of the GMS.

7.1 Optical device housings

A special housing for the Proximity was developed for ATLAS. A picture of it is shown in Fig. 23. This housing, called the Proximity telescope, houses the CCD sensor, its driving electronics (shown in Fig. 19) and a lens. An infrared filter was added in order to prevent the CCD to be blinded by visible light. This tube has a diameter of 30 mm and a length of 19 cm. The distance between the CCD and the lens can be adjusted in order to have the image of the mask focused on the CCD.
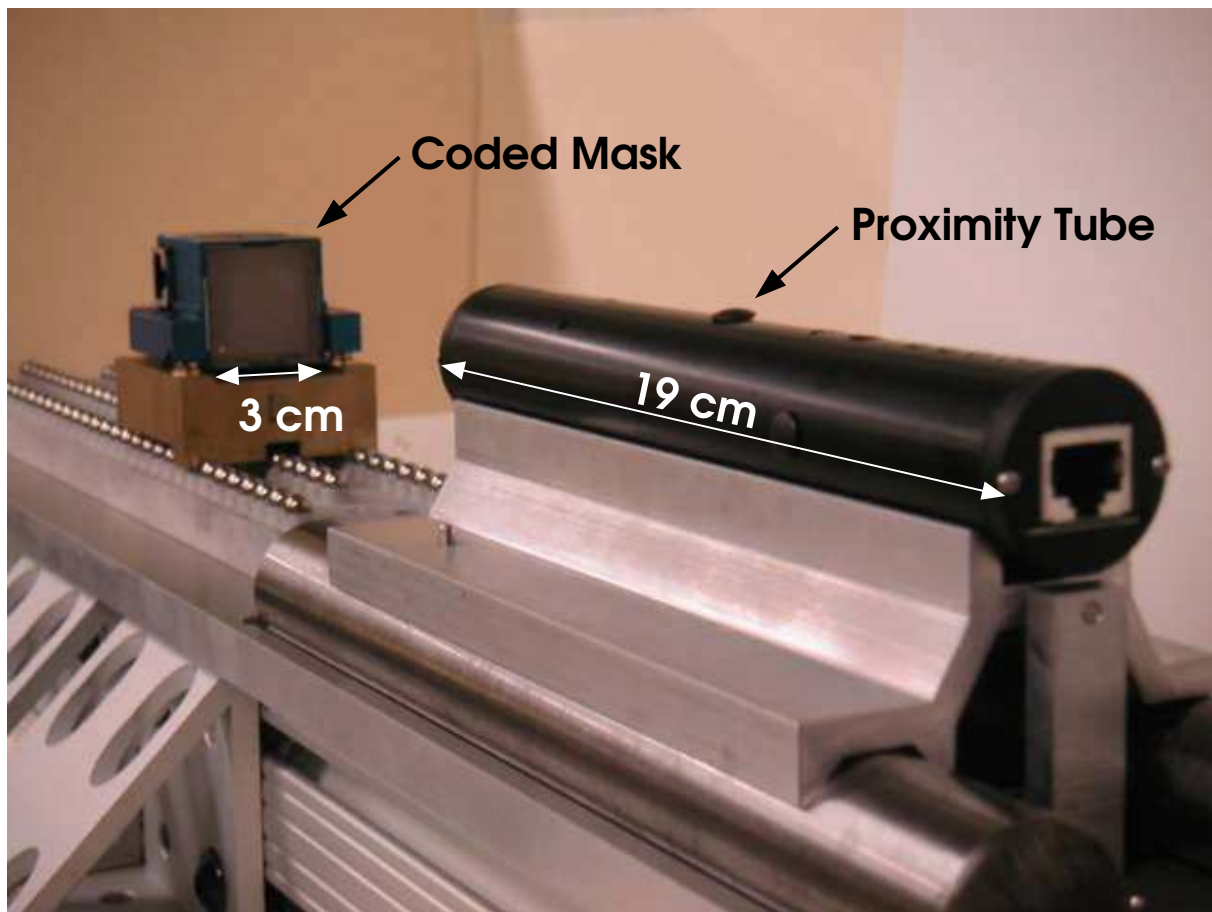

Figure 23: Picture of the Proximity telescope which houses the CCD sensor, the lens and in the back a coded mask.

7.2   Passing through the support of the dipole coils

Figure 24 shows the passage of the BCAM optical lines between the stations 3 and 4 through the supports of the dipole coils. Holes through each support are needed. There are two constrains regarding the position of the hole:
- the hole should be between two fins of the support,
- the hole should avoid the welding of the fins.

After the first assembly of the dipole in the cavern, the exact position of the coil supports were measured. These measurements will be used to reposition the coil support in the Euclid drawings. From that point the positions of the holes needed for the optical lines will be adjusted.
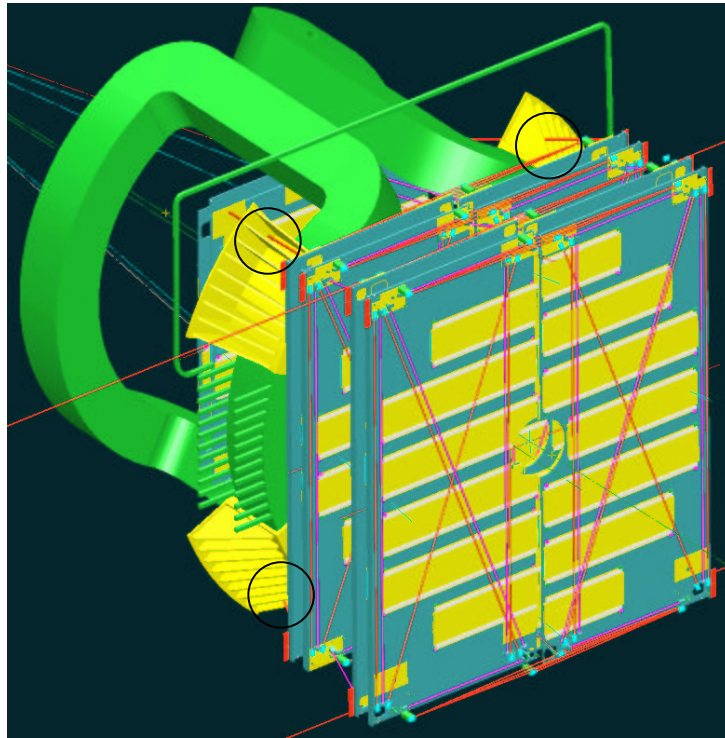

Figure 24: Mechanical drawing showing the passing of optical lines between stations 3 and 4 through the supports of the dipole coils. Note: the tubes are not real elements but only volume to be kept free for the light rays.

7.3   Mechanical fixation and adjustment of the platforms

Figure 25 shows a schematic of a platform supporting the optical devices. The platforms are fixed on three points. A screw allows us to adjust the distance between the platform and the chamber support. The connection between the platform and the chamber is done by a ball-and-socket joint.
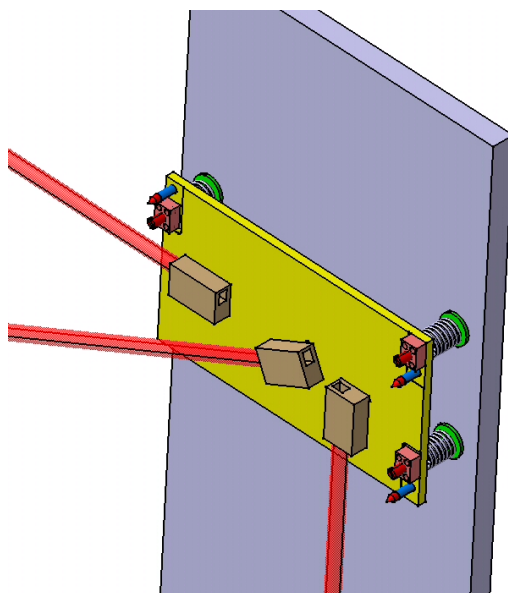
Figure 25: Schematic of a platform supporting the optical devices.

7.4 Links to the walls

Figure 26 shows a 3 dimension view of the optical lines linking the chamber 9 to the walls of the cavern. The fixation points on the wall are at the same Z that the platforms of the chamber 9.
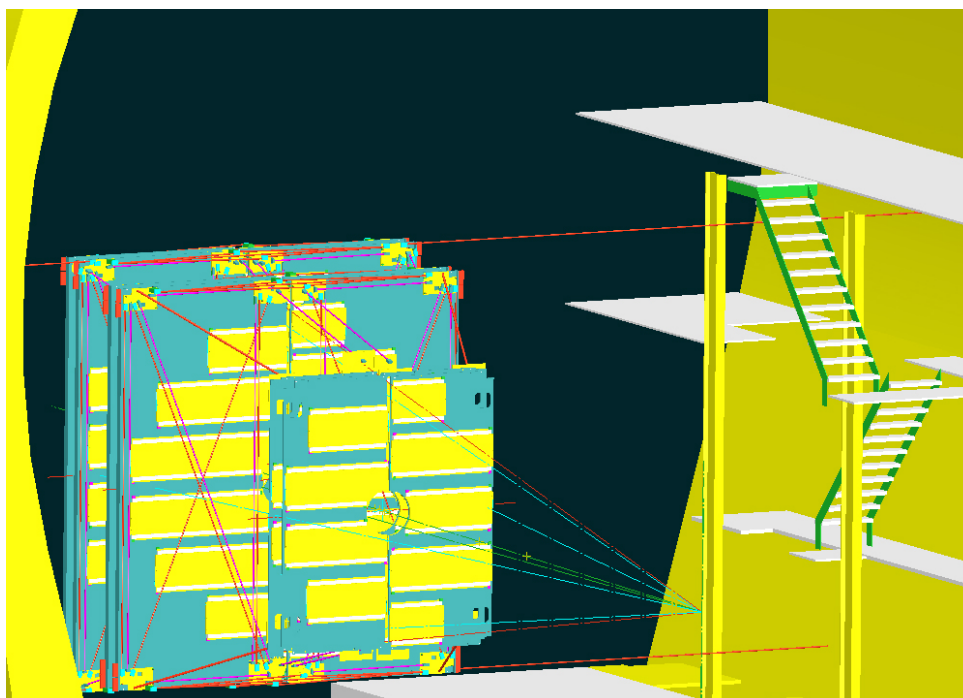

Figure 26: Mechanical drawing showing the optical lines linking the chamber 9 to the walls of the cavern.

8 Operational procedures

8.1 Platform alignment procedure

An alignment of the platforms of a given chamber (for stations 1 and 2) or a given half chamber (stations 3 to 5) will be performed in order to:
- place all platforms of a chamber in a common plan,
- place this common plan parallel to the plan of the chamber support.

In this way we will be able to determine the position of the chamber support knowing the position of the optical elements.

With the help of the CERN survey group we will align one of the four platforms relative to the support plan. The photogrammetry will be the technique used to perform this alignment. It consists of taking pictures of an object from different points and of treating the 2D images in order to recalculate the geometry of the object. The typical resolution of this method is of the order of 50 μm [17] which gives a resolution of 250 μrad in the angle between the two plans.
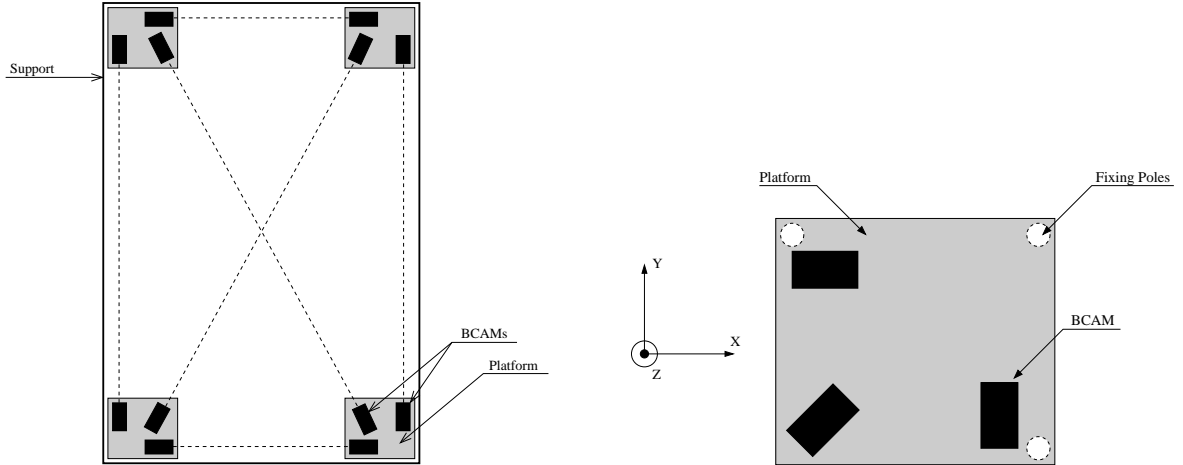

Figure 27: **Left:** Setup which will be used to align the platform of a given support, **right:** Details of one platform.

After the positionning of one of the platform, we will align the three other ones with respect to the first one using an array of BCAM devices as shown in figure 27-left. Each platform will be mounted on three poles (see figure 27-right) which will give the possibility to adjust their distance to the support.

By simulation, we obtained the achievable accuracies that we can expect from this setup. Table 5 gives a summary of this simulation. In average, we can align all four platforms to within 65 μrad. The alignment in Z is largely depending on the distance between the platforms, which explains why it is becoming worse as the station get bigger. All these resolutions are mostly due to a systematic error in the positioning of the BCAMs on the platform. For this simulation, we took a commonly admitted "installation accuracy" of 50 μrad and 50 μm [18]. These resolutions are bigger than the ones shown in table 3. It is

due to the fact that in the section 3.2.1, we were interested in the relative displacement of the platforms between two measurements (in other words the monitoring of the position of the platforms). In the "relative measurements" configuration, the positioning accuracy of the BCAMs does not affect the resolution. Here, it is the biggest contribution to the "absolute measurement" configuration.

Station	σ_{θ_x} (μrad)	σ_{θ_y} (μrad)	σ_z (μm)
1	68	68	88
2	64	65	98
3	57	67	105
4	56	68	148
5	56	68	161

Table 5: Resolution achievable in the platform alignment using an array of BCAM.

8.2 Installation and monitoring procedures

Platforms will be mounted on the chamber supports after the installation of the electronics on the entire chamber. Platforms will be aligned using (as described in the previous section) an array of 6 BCAM lines per chamber (or half chamber for stations 3 to 5).

Then, the survey group of CERN will measure the positions of all optical elements with respect to the slates using the photogrammetry [17]. Using this technique, we are able to position the elements to 50 μm. An image of all optical lines will be taken at this stage. An image of all optical lines will be taken after the installation of the chamber inside the cavern and will be compared to the first one in order to detect any movement of the platforms during the transport from the assembly hall to the cavern.

With the first beam in the LHC, the entire spectrometer will be aligned using straight muon tracks (the dipole magnet will be switched off). During this "calibration" run, an image of all the optical lines will be taken. These images, being correlated with the initial position of the chambers, will be kept as references. It means that our system will measure the displacement of the chamber supports relative to this reference position.

After the installation and the alignment of the spectrometer, our system will be ready to monitor the displacements and the deformations of the chamber supports. After switching on the magnet, images from all optical lines will be periodically recorded during the physics runs and compared to the references. Image displacements will be extracted. From these image displacements, we will be able to extract chamber displacements and deformations using the MINUIT fitter.

8.3   Cabling

The cabling schemes adopted for the two configurations are shown in Fig. 28 (for stations 1 and 2) and in Fig. 29 (for stations 3 to 5). We need to use 4 multiplexers per tracking chamber for station 1 and 2, and 6 multiplexers per chamber for stations 3 to 5. Two other multiplexers will be used for the BCAMs which are fixed to the wall of the cavern (one multiplexer on each side). In total, we will use 54 multiplexers. As each driver board provides 8 input/output sockets resulting in a need of 7 drivers. As mentioned in section 5, each multiplexer provides 10 input/output branch sockets. A total of 468 active elements will be connected.
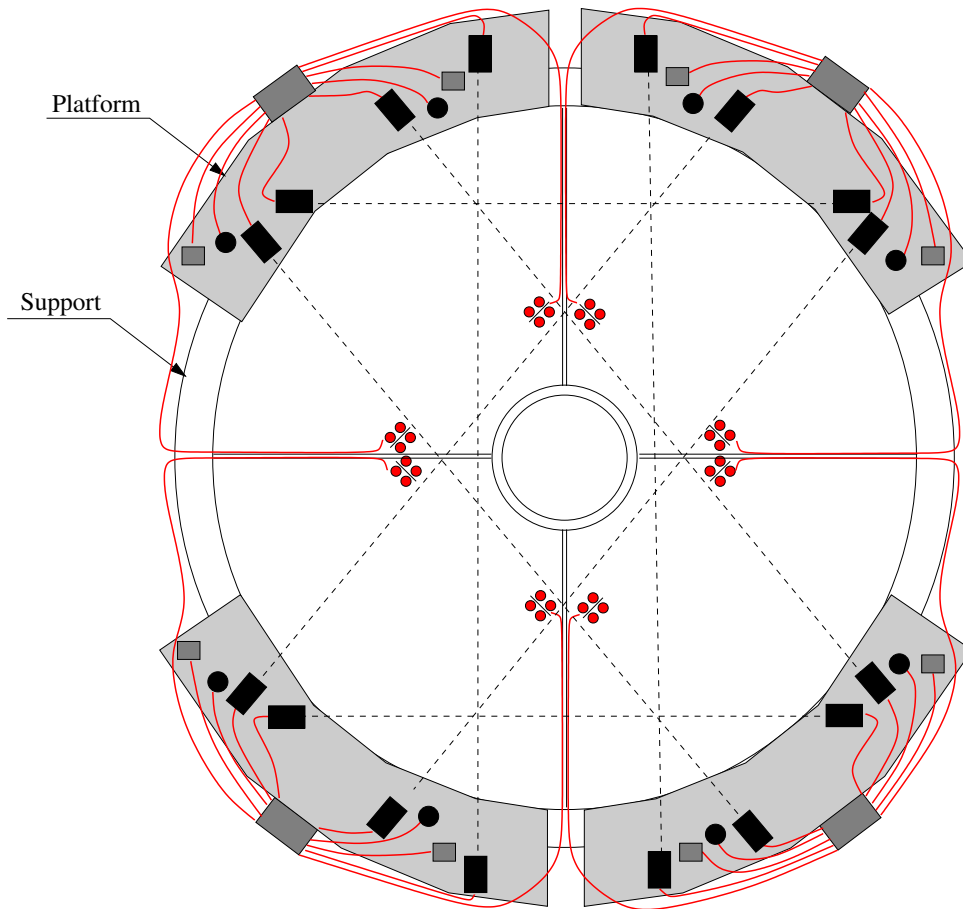

Figure 28: Cabling scheme for a chamber of stations 1 and 2

There are two types of cables: the branch cables which connect the devices to the multiplexers and the root cables which connect the multiplexers to the drivers. The cables used are non-standard Category 5 type cables. The standard Cat-5 cables which are used for network connection have 8 data wires twisted together in four pairs. The cables used for the GMS have to carry four low voltages (0 V, 5 V and ±15 V) to the devices, should allow the transmission of the commands from the drivers up to the devices and should also allow the reception of the images from the CCD down to the drivers. Therefore, the wires inside the cables have to be separated as follows: two twisted pairs of data wires
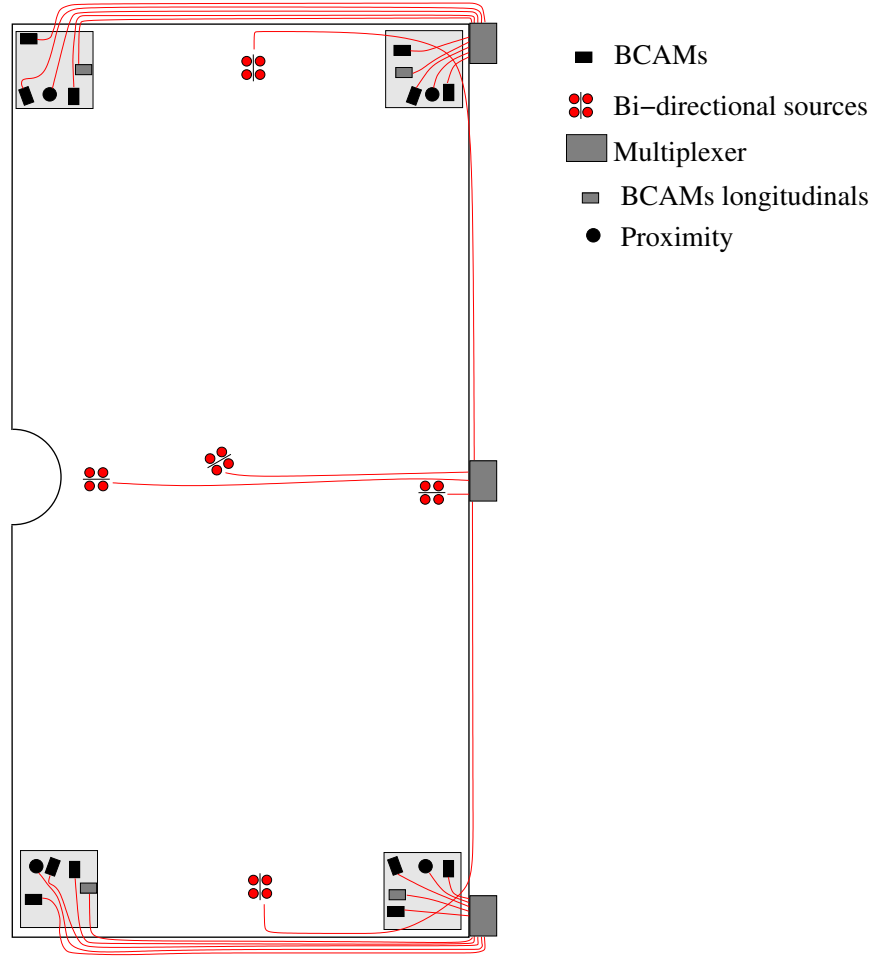
Figure 29:   Cabling scheme for half a chamber plan of stations 3 to 5.

and four power-carrying wires which are not twisted together. ATLAS collaborators order
such cables from "Quabbin Wire and Cable". A full description of the cable parts and the
procedure how to make the cables is given in reference [19].

The difference between the root and the branch cables rests in the conductor type. In the
case of root cables, the core is solid in order to minimize the attenuation. These cables
can be up to 140 meters long. The branch cables core is stranded. Therefore, these cables
are flexible but the attenuation being bigger they can only be up to 20 meters long.

8.4   Numbering scheme

Each BCAM box, Proximity telescope, coded mask and bi-directional sources (including
the spare devices) will receive an unique name which will be for:

- BCAM: BCAM001 to BCAM326,
- Proximity telescope: PROX001 to PROX044,
- coded mask: MASK001 to MASK044,
- bi-directional sources: SOUR001 to SOUR102.

A database will be filled with the specifications and/or calibration constants of each el-
ement. When used, it will be associated with the name of the optical line for which this

device will be used.

We developed a numbering scheme which allows us to unambiguously name all optical lines and all optical element position. This numbering scheme is complying with the ALICE note [20].
(1) One letter gives the optical line type (**P** = Proximity, **B** = BCAM),
(2) Three characters give the support which holds the CCD sensor:
   - For chambers: chamber 1 = **CH1**, chamber 2 = **CH2**, ..., chamber 10 = **CH10**
   - If the support is on the wall of the cavern, the code is **WAL**
(3) One number gives the platform number on that support (see figure 30),
(4) Three characters give the support which holds the mask or the laser diodes,
(5) One number gives the platform number on that support,
(6) Finally one number gives the image number, always 0 for Proximity, 0 to 5 for BCAM. Lasers 0 and 1 will be the lasers of the opposite box (see figure 30-bottom-right for the laser number), and lasers 2 to 5 will be the number of the lasers of the bi-directional sources on a given BCAM transverse line.

The next step is to name all the devices of each line. In order to do so, one character is added to the name of the line in order to name the CCD (C), the laser diode (L) or the mask (M) of this given optical line.
Finally, a last character is added in order to name the cable (C) connected to this device and the support (S) on which the device is fixed.

This numbering scheme is fully working because there is only one line of each type (Proximity or BCAM) linking two different platforms. The chambers of station 1 and 2 are equipped with 4 platforms, but we artificially go back to 8 platforms by cutting them (see figure 30-bottom-left).

Let us give few examples:
(1) **B_CH23_CH33_1**: will name the BCAM line which is part of the longitudinal monitoring and which links the platforms #3 of chambers #2 (station 1) and #3 (station 2). The CCD sensor is on the chamber 2 and the laser #1 of the opposite BCAM box is ON.
(2) **B_CH23_CH33_1_L**: will name the Laser of the BCAM line described above.
(3) **B_CH97_WAL0_1**: will name the BCAM line which is part of the external monitoring and which links the platforms #7 of chamber #9 to the platform #0 of the wall of the cavern. The CCD sensor is on the chamber and the laser #1 of the opposite BCAM box is ON.
(4) **P_CH11_CH21_0**: will name the Proximity line which is part of the longitudinal monitoring and which links the platforms #1 of chambers #1 and #2 (station 1). The CCD sensor is on the chamber 1.
(5) **P_CH11_CH21_0_M**: will name the coded mask of the above optical line.
(6) **P_CH11_CH21_0_M_C**: will name the cable attached to this coded mask.
(7) **B_CH63_CH64_2**: will name the BCAM line which is part of the transverse monitoring and which links the platforms #3 and #4 of the chamber #6. The CCD is on
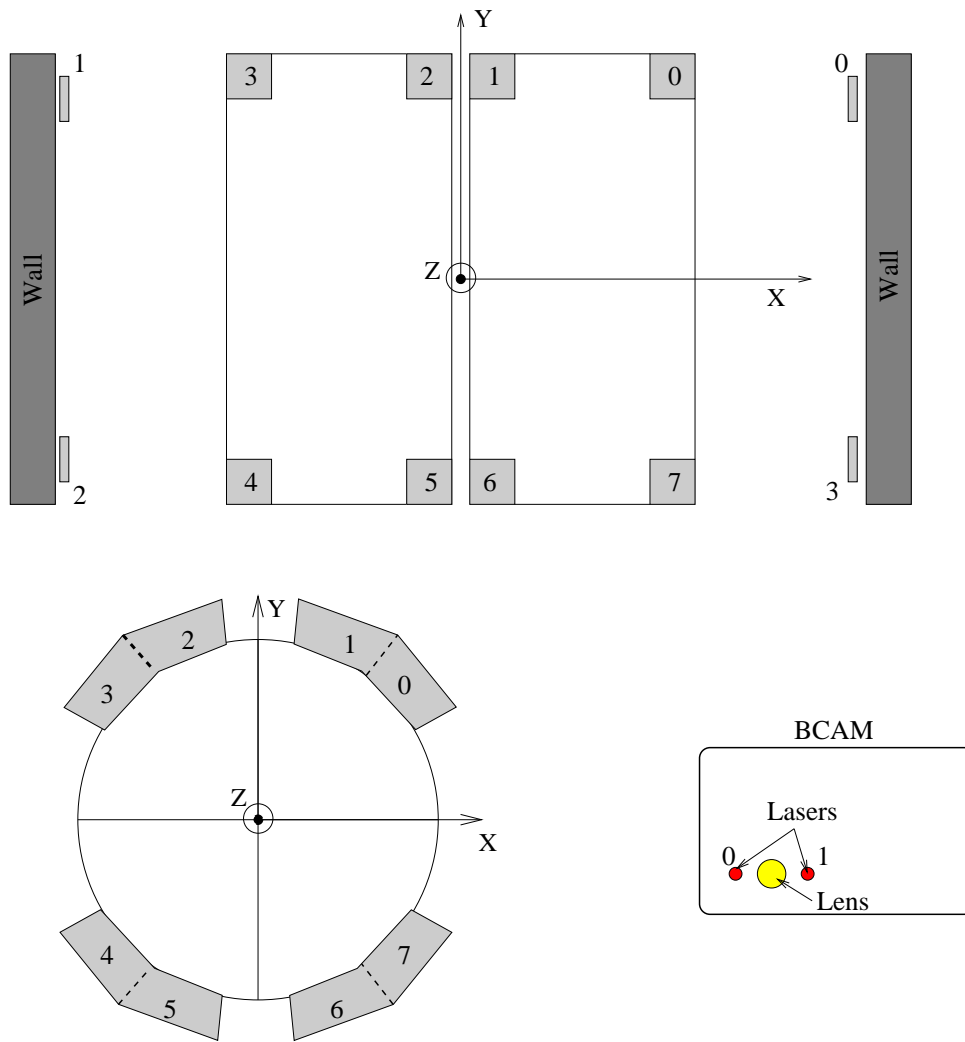
Figure 30: Numbering schemes of the platforms holding the optical elements and numbering of the Lasers of a BCAM (bottom right).

the platform #3 and the left laser of the bi-directional source is ON.

(8) **B_CH63_CH64_2_L_C**: will name the cable of that bi-directional source.

9 Tests

In order to fully validate the setup of the GMS and the simulation software which has been developed, a series of tests are and will be performed in laboratory.

9.1 Test of the temperature gradient effects

The first tests were performed on a single BCAM optical line in order to determine the effects of thermal fluctuations on the resolution of the BCAM. Figure 31 shows the
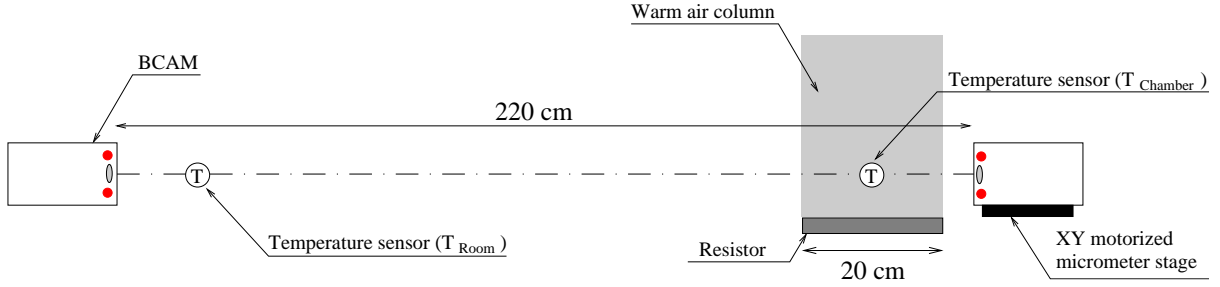

Figure 31: Schematic view of the system used to test the effect of thermal gradient on the BCAM resolution.

system we used for these tests. On an optical table, we set-up a BCAM line with one of the BCAM box fixed on a XY motorized micrometer stage. In front of one of the two BCAM we placed a resistor plate. It creates a warm air column which mimics the warm air which will be provided by the electronics of the tracking chambers.

The thermal specifications for the tracking chambers of the dimuon spectrometer are as follows:

  - air maximum temperature: $T_{max} = 40$ °C,
  - air maximum thermal gradient: $\Delta T_{max} = 20$ °C.

Simulation of cooling of the tracking chambers shown that these requirements will be reached [21].

During our tests, we modified the output power of the resistor in order to reach several temperature differences ($\Delta T = T_{warm\ air} - T_{room}$) between the warm air temperature ($T_{warm\ air}$) and the room temperature (T_{room}).

Figure 32 shows the resolution of the BCAM obtained during these measurements as a function of the temperature difference ($\Delta T = T_{warm\ air} - T_{room}$). The filled circles on that figure give the resolution obtained with the setup described in Fig. 31. We clearly see that the resolution of the BCAM deteriorates as the temperature difference increases. At the thermal gradient given by the specification ($\Delta T = 20$ °C), the resolution of the BCAM is of the order of 3 μm which is about 6 times bigger than the intrinsic resolution of that device (see section 2.3).

From our simulations (see section 4), we saw that, in order to have a sagitta resolution below 70 μm, the resolution of the BCAMs should be below 4 times the intrinsic resolution (see figure 14-top-right). The best solution we found during our laboratory tests in order
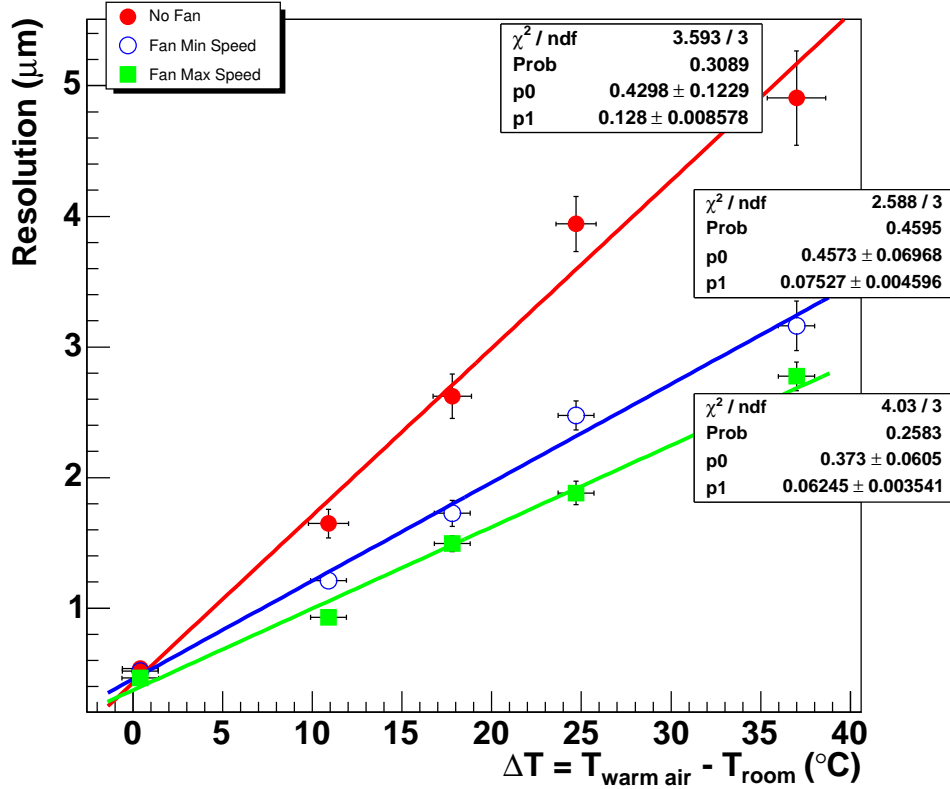
Figure 32: Resolution of a BCAM as a function of the temperature difference ΔT between the room and the warm air column in front of the chamber without (filled circles) and with (opened circles and grey squares) cold air blowning.

to reduce the effects of thermal fluctuations on the BCAM resolution (solution which have been confirmed by our ATLAS collaborators) is to blow "cold" air on the warm zone (see Fig. 33). The air was not really cold. We just blew air at room temperature using a standard fan. We did measurements at two different fan speeds. The results of these measurements can be seen on figure 32. In this figure, the opened circles correspond to the minimum fan speed, the squares to the maximum fan speed (the filled circles are the result without any fan). One can see that blowing air in front of the BCAM reduces the effect of the thermal gradient and thermal fluctuation. Moreover, this reduction is larger if the air flow increases. It is difficult to give a quantitative answer concerning the results of these tests as we do not have any way to know the absolute value of the air flow. But we can see that with a standard fan, blowing air at room temperature, allows to reduce the effect of thermal fluctuation by a factor 2.

We know that cold air at 15 °C will be blown on the tracking chambers in order to keep the temperature below the maximum temperature allowed by the specifications ($T_{max} = 40$ °C). Diffusers will be placed at the top of each station. Station 3, which is inside the dipole magnet, will be treated differently by sending in addition cold air from the bottom of the chambers. Our optical elements are placed in the corners of the
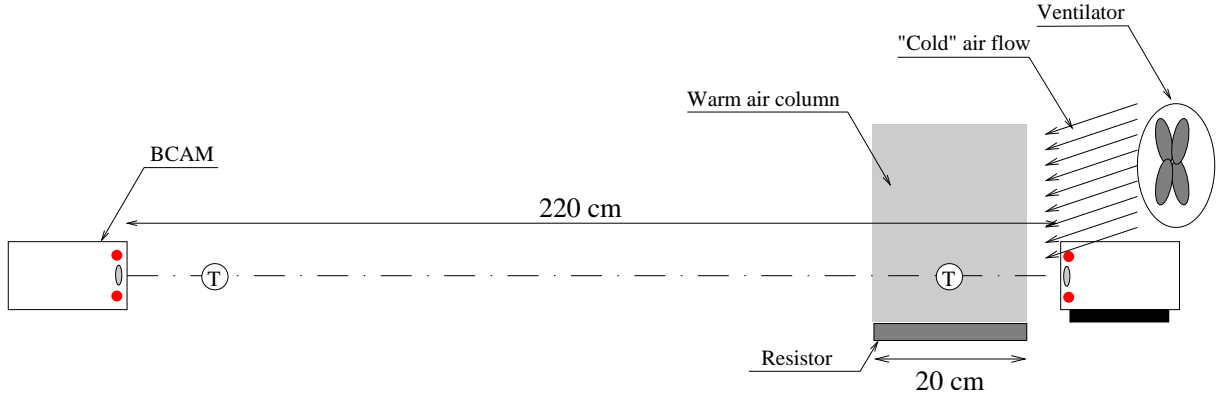
Figure 33: Schematic view of the setup used to test the effect of blowing "cold" air in order to reduce effects due to the thermal gradient on the BCAM resolution.

chambers. Therefore, they will directly benefit from the cold air flow used to cool down the chambers electronics.

From our tests we were able to contained the resolution of the BCAM at 1.5 μm which is three times its intrinsic resolution (see figure 32). We can also notice that at this value, the resolution on the mass coming from the GMS is of the order of 15 MeV/c^2 (see figure 14-bottom-left). Therefore, we can conclude that even in the temperature environment of the dimuon spectrometer the GMS will achieve its requirements.

9.2   Platform alignment

A first test bench is devoted to the study of the platform alignment procedure. As we described it in section 8.1, an alignment of the platforms of a same chamber (or half a chamber for stations 3 to 5) should be made. In order to confirmed the result of the simulation, we decided to built a test bench made of four platforms. Figure 34 shows a schematic of this test bench. It reproduces the dimensions of the biggest plan (i.e. half a chamber of station 5) for which the difficulty of alignment is maximum. The four platforms are fixed to a rigid reference (wall of the room), and three adjustment screws allow us to change the orientation of the platforms around both X and Y axis as well as their distance to the support.
Using this test bench we confirmed the installation procedure of the optical elements on the platforms. We also confirmed the results of the simulation given in section 3.2.2 which predicted that we should be able to align the platforms of on chamber of station 5 at the level of 30 μm and 8 μrad.

9.3   Validation of the simulation

A second test bench will be a mock up of 3 chambers (chambers 6 to 8). Figure 35 shows a schematic of this test bench. Its aim is to test our ability to retrieve the displacement of the chambers and to evaluate the effects of temperature gradient in the way of the optical lines. In order to do so, mechanisms will be developed to move the chambers at
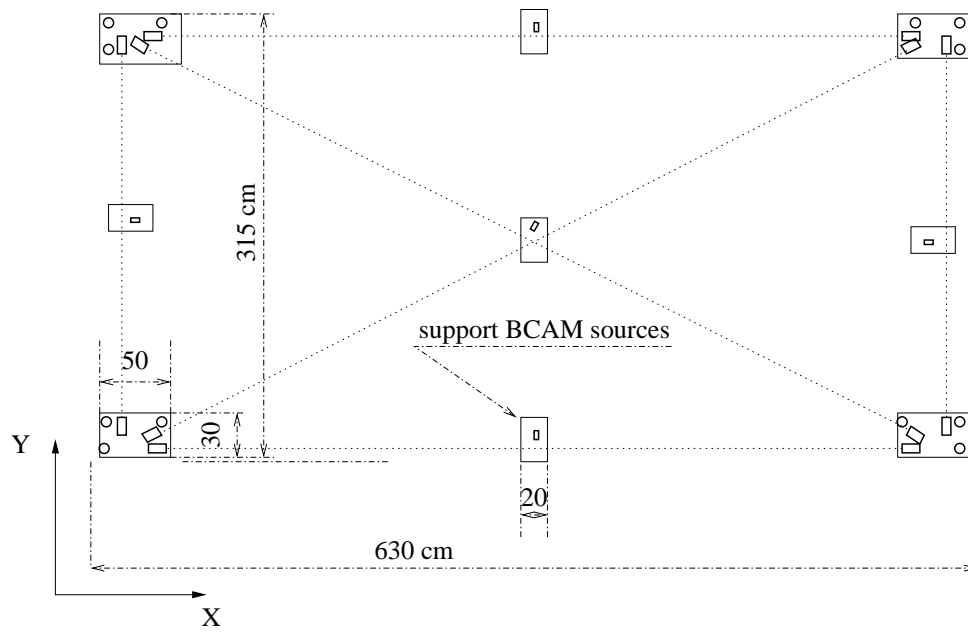
Figure 34: Schematic of the test bench devoted to the study of the platform alignment procedure.

a few micron level and to provide local temperature increase. The chambers 6 and 7 will be linked using 4 BCAM lines. The chambers 7 and 8 will be linked using 4 Proximity devices. In a longer term, this bench will also be used to developed the acquisition system of the GMS which should be added to the DCS.

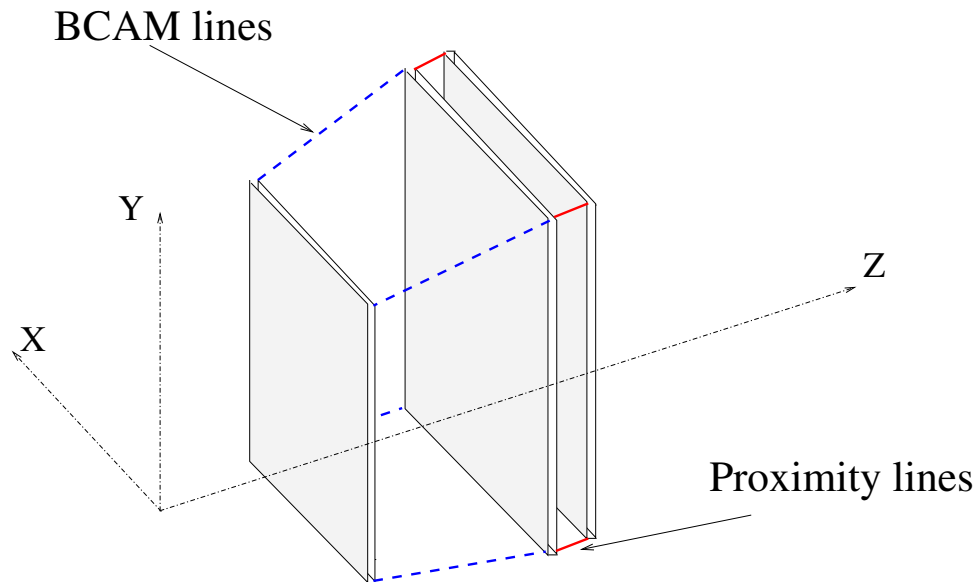Figure 35: Schematic of the test bench which mocks up 4 chambers.

10 Conclusion

10.1 Planning

The construction of the elements can start in the first quarter of 2005 and should be completed in about 9 months. Therefore, we should be able to deliver the optical elements to CERN during the last quarter of 2005. In the mean time, our ATLAS collaborators agreed to lend us the elements needed for our test bench in Lyon.

The installation planning of the GMS is highly correlated to the planning of the tracking chamber mounting. Two different strategies will be used: one for the stations 1 and 2, and the other for the stations 3 to 5. For stations 1 and 2, the Orsay group plans to have a first installation of a chamber in their laboratory. We will have the opportunity to do the first installation of our system, and also to experiment the alignment procedure (described in section 8.1) for the platforms. Then the chambers will be dismounted and sent to CERN for their final installation. There, we will mount again our system and realign the platforms with the experience of the first installation in Orsay. Then the chambers will be installed in the cavern where no more adjustment should be needed. A complete check of the platform alignment will be done in order to check if some elements moved during the transport from the installation hall to the cavern.

For stations 3 to 5 the situation is a little bit different in the sense that no installation is foreseen before the final installation of the slat on their support at CERN. Therefore, we will directly do the final installation of our system at CERN according to the installation planning of the chambers of stations 3 to 5.

	2005				2006				2007			
Quarter	1	2	3	4	1	2	3	4	1	2	3	4
Optics elements	F	FL	FL	FL	MC	MC	C	C	C			
Supports	F	F	FL	FL	M	M	C	C	C			
Platforms	F	F	FL	FL	M	M	C	C	C			
Stations 1 and 2	A	A	LA	L	M	MC	C	C	C			
Stations 3 to 5	A	A	A	A	M	MC	C	C	C			

Table 6: Planning of the GMS construction and commissioning. The meaning of the letters is: F = Fabrication, A = Assembly, L = Local commissioning, M = on site Mounting and C = CERN commissioning.

Table 6 gives an overview of the planning of the GMS construction, mounting and commissioning. The last two lines of this table give the planning of the tracking stations in the same period. As mentioned above, the planning of the GMS is strongly correlated to the planning of the tracking chambers. In particular, we can see that the mounting on site at CERN starts in the second half of 2005 which is the time when the tracking

chambers of stations 3 to 5 will start to be assembled at CERN. The final mounting of tracking chambers of stations 1 and 2 is planned for the first semester of 2006. But the mounting of these chambers in Orsay is scheduled for the second and third trimesters of 2005. Therefore, the fabrication of supports and platforms should start with the ones related to stations 1 and 2 in order to be ready for the mounting in Orsay of the optics elements.

10.2   Cost estimate

All the optical devices will be order to the compagny named Open Source Instrument Inc. (OSI) which has been created by ATLAS collaborators who developed the BCAM system. An evaluation of the total price of the GMS is given in table 7. The total cost is estimated to 252 kCHF.

Label	Units	Spare units	Unit price ($)	Total Price ($)	Total Price (CHF)
Simple BCAM	264	26	260	75400	
Double BCAM	24	2	500	13000	
Design of Bi-directional	1		5000	5000	
Bi-directional sources	92	10	150	15300	
Proximity	40	4	325	14300	
Driver board	7	1	650	5200	
Multiplexer	54	6	130	7800	
Cables				9900	
OSI contribution				50000	
Total OSI				195900	232180
Mechanics					20000
Total					**252180**

Table 7: GMS estimated cost. We used 1 CHF = $0.84374 as change ratio between Swiss Franc and US Dollar (change of January 28th 2005).

Acknowledgements

References

[1] A. Morsch:
The Muon Arm Simulation and Reconstruction Package in AliRoot:
http://morsch.home.cern.ch/morsch/MUONdoc/Contents.html

[2] The ALICE offline Project
http://AliSoft.cern.ch/offline/

[3] S. Grigoryan et al.:
Using Muons to Align Tracking Chambers in the ALICE Dimuon Forward Spectrometer,
ALICE Internal Note ALICE-INT-2003-051.

[4] A. Grigoryan et al.:
Reconstruction of Muon Tracks for Alignment of Tracking Chambers of the ALICE Dimuon Forward Spectrometer,
PREPRINT YerPhI 1594(4) - 2004.

[5] H. van der Graaf, H. Groenstege, C. Guyot, F. Linde and P. Rewiersma:
RasNiK, an alignment system for the ATLAS MDT barrel muon chambers,
NIKHEF Internal Note ETR-2000-04.

[6] H. Gulkanyan:
Apparent sagitta measurement with RasNiK,
Internal report of YerPhi/ ALICE group (1999).

[7] K. Hashemi and J. Bensinger:
The BCAM camera,
ATLAS Internal Note ATL-MUON-2000-024.

[8] P. Pillot et al.:
The Geometry Monitoring System of the ALICE Dimuon Spectrometer - Simulation results,
ALICE Internal Note to be published.

[9] C. Lasseur: *Private communication.*

[10] G. Dicker:
Linearity, Resolution, and Systematic Errors of the CCD - RASNIK Alignment System,
Nikhef Internal Note (1997).

[11] A.A. Grigoryan and A. Teimurazyan:
Light ray displacements due to air temperature gradients,
ALICE Internal Note ALICE-INT-2000-13.

[12] Texas Instruments:
The CCD image sensor TC255P,
http://focus.ti.com/lit/ds/symlink/tc255p.pdf

[13] K. Hashemi and J. Bensinger:
Irradiation of the TC255P CCD by fast neutrons,
ATLAS Internal Notes ATL-MUON-98-253 and ATL-MUON-2000-01.

[14] A. Morsch and B. Pastircak:
Radiation in ALICE detectors and electronics racks,
ALICE Internal Note ALICE-INT-2002-028.

[15] H. van der Graaf and H. Groenstege:
The radiation hardness of RasNiK components for the ATLAS muon barrel spectrometer,
ATLAS Internal Note ATL-ELEC-2002-002.

[16] K. Hashemi:
Radiation tolerance of end-cap alignment electronics,
ATLAS Electronics Production Readiness Review (2003).

[17] C. Lasseur:
Métrologie de positionnement appliquée aux détecteurs,
EDMS Note 362063 (2002).

[18] K. Hashemi:
BCAM user manual,
http://alignment.hep.brandeis.edu/ATLAS/Devices/bcam_user_manual.pdf (2003).

[19] K. Hashemi:
ATLAS Branch Cables,
http://alignment.hep.brandeis.edu/ATLAS/Electronics/ATLAS_Branch_Cables.pdf

[20] L. Betev and P. Chochula:
Definition of the ALICE coordinate system and basic rules for sub-detector components numbering,
ALICE Internal Note ALICE-INT-2003-038.

[21] S. Salasca:
Progress on cooling of stations 3, 4 and 5,
Dimuon meeting, Torino (2003).

[22] A. Schricker:
The alignment system of the ATLAS muon end-cap spectrometer,
Doctorat Thesis, Vienna university of Technology (2002).